

**TTL dehydration**

F. Hasebe et al.

This discussion paper is/has been under review for the journal Atmospheric Chemistry and Physics (ACP). Please refer to the corresponding final paper in ACP if available.

# Cold trap dehydration in the Tropical Tropopause Layer characterized by SOWER chilled-mirror hygrometer network data in the Tropical Pacific

F. Hasebe<sup>1</sup>, Y. Inai<sup>2</sup>, M. Shiotani<sup>3</sup>, M. Fujiwara<sup>1</sup>, H. Vömel<sup>4</sup>, N. Nishi<sup>5</sup>,  
S.-Y. Ogino<sup>6</sup>, T. Shibata<sup>7</sup>, S. Iwasaki<sup>8</sup>, N. Komala<sup>9</sup>, T. Peter<sup>10</sup>, and S. J. Oltmans<sup>11</sup>

<sup>1</sup>Faculty of Environmental Earth Science, Hokkaido University, Sapporo, Japan

<sup>2</sup>Graduate School of Science, Tohoku University, Sendai, Japan

<sup>3</sup>Research Institute for Sustainable Humanosphere, Kyoto University, Uji, Japan

<sup>4</sup>GRUAN Lead Center, Meteorologisches Observatorium Lindenberg, Lindenberg, Germany

<sup>5</sup>Geophysical Institute, Kyoto University, Kyoto, Japan

<sup>6</sup>Japan Agency for Marine-Earth Science and Technology, Yokosuka, Japan

<sup>7</sup>Graduate School of Environmental Studies, Nagoya University, Nagoya, Japan

<sup>8</sup>National Defense Academy, Yokosuka, Japan

<sup>9</sup>Lembaga Penerbangan dan Antariksa Nasional, Bandung, Indonesia

<sup>10</sup>Eidgenössische Technische Hochschule Zürich, Switzerland

<sup>11</sup>Earth System Research Laboratory, NOAA, Boulder, CO, USA

25833

Title Page

Abstract

Introduction

Conclusions

References

Tables

Figures

◀

▶

◀

▶

Back

Close

Full Screen / Esc

Printer-friendly Version

Interactive Discussion



Received: 7 September 2012 – Accepted: 13 September 2012  
– Published: 28 September 2012

Correspondence to: F. Hasebe (f-hasebe@ees.hokudai.ac.jp)

Published by Copernicus Publications on behalf of the European Geosciences Union.

ACPD

12, 25833–25885, 2012

## TTL dehydration

F. Hasebe et al.

Title Page

Abstract

Introduction

Conclusions

References

Tables

Figures



Back

Close

Full Screen / Esc

Printer-friendly Version

Interactive Discussion



## Abstract

A network of balloon-born radiosonde observations employing chilled-mirror hygrometers for water and electrochemical concentration cells for ozone has been operated since late 1990s in the Tropical Pacific trying to capture the progress of dehydration for the air parcels advected horizontally in the Tropical Tropopause Layer (TTL). The analyses of this dataset are made on isentropes taking advantage of the conservative properties of tracers in adiabatic motion. The existence of ice particles is diagnosed by lidars simultaneously operated with sonde flights. Characteristics of the TTL dehydration are presented on the basis of individual soundings and statistical features. Supersaturations close to 80 % in the relative humidity with respect to ice ( $RH_{ice}$ ) have been observed in subvisible cirrus clouds located near the cold point tropopause at extremely low temperatures around 180 K. Further observational evidence is needed to confirm the credibility of such high values of  $RH_{ice}$ . The progress of TTL dehydration is reflected in isentropic scatter plots between the sonde-observed mixing ratio (OMR) and the minimum saturation mixing ratio ( $SMR_{min}$ ) along the back trajectories associated with the observed air mass. The supersaturation exceeding the critical value of the homogeneous ice nucleation ( $OMR > 1.6 \times SMR_{min}$ ) is frequently observed on 360 and 365 K surfaces indicating that the cold trap dehydration is under progress in the TTL. The near correspondence between the two ( $OMR \sim SMR_{min}$ ) on 380 K on the other hand implies that this surface is not significantly cold for the advected air parcels to be dehydrated. Above 380 K, the cold trap dehydration would scarcely function while some moistening in turn occurs before the air parcels reach the lowermost stratosphere at around 400 K where OMR is generally smaller than  $SMR_{min}$ .

## 1 Introduction

The understanding of the stratospheric dryness starts from the idea that it must reflect the temperature history the air experienced before entering the stratosphere (Brewer,

ACPD

12, 25833–25885, 2012

## TTL dehydration

F. Hasebe et al.

Title Page

Abstract

Introduction

Conclusions

References

Tables

Figures

◀

▶

◀

▶

Back

Close

Full Screen / Esc

Printer-friendly Version

Interactive Discussion



**TTL dehydration**

F. Hasebe et al.

[Title Page](#)[Abstract](#)[Introduction](#)[Conclusions](#)[References](#)[Tables](#)[Figures](#)[Back](#)[Close](#)[Full Screen / Esc](#)[Printer-friendly Version](#)[Interactive Discussion](#)

1949; Newell and Gould-Stewart, 1981; Danielsen, 1982). Among many hypotheses, the “cold trap” theory in which air parcels are dehydrated during quasi-horizontal advection in the tropical tropopause layer (TTL) of the Western Tropical Pacific (Holton and Gettelman, 2001) is becoming widely accepted as one of the key dehydration processes. Thin cirrus clouds, too thin to be visually detectable and often called subvisible cirrus clouds (SVCs; Jensen et al., 1996), are frequently observed even far from tropical convective systems (Winker and Trepte, 1998) suggesting that they are related to the “cold trap” dehydration.

Aircraft observations such as those conducted during the Pre-AVE campaign have revealed water vapour profiles with high vertical resolution (Richard et al., 2006) over the tropical Central America. The Lagrangian temperature history along trajectories for those air parcels observed has been conveniently used to study the efficiency of dehydration (e.g. Jensen and Pfister, 2004; Fueglistaler et al., 2004, 2005; Fueglistaler and Haynes, 2005). Such an approach proved to be quite successful as compared to the Eulerian description in reproducing the water vapour field from meteorological data (e.g. Liu et al., 2010; Schoeberl and Dessler, 2011). The effectiveness of trajectory-based estimation of the dehydration efficiency, however, still awaits support from observational data. What is missing in such studies is the in situ water vapour data in the TTL over the Western Tropical Pacific where the “cold trap” dehydration is supposed to be taking place.

The Soundings of Ozone and Water in the Equatorial Region (SOWER) project (Hasebe et al., 2000) is intended to accumulate ozone and water vapour profiles in the troposphere and the lower stratosphere (LS) in the Tropical Pacific by radiosonde observations (Vömel et al., 2002). It has been operating chilled-mirror hygrometers such as NOAA frostpoint hygrometer (FPH; Vömel et al., 1995), Snow White (SW; Fujiwara et al., 2003; Vömel et al., 2003) and the University of Colorado Cryogenic Frostpoint Hygrometer (CFH; Vömel et al., 2007a) to accurately measure water vapour profiles since 1998. These data constitute the basis to describe the seasonal to decadal variations of TTL/LS water vapour in the tropics (Fujiwara et al., 2010).

## TTL dehydration

F. Hasebe et al.

[Title Page](#)[Abstract](#)[Introduction](#)[Conclusions](#)[References](#)[Tables](#)[Figures](#)[◀](#)[▶](#)[◀](#)[▶](#)[Back](#)[Close](#)[Full Screen / Esc](#)[Printer-friendly Version](#)[Interactive Discussion](#)

The efficiency of the “cold trap” dehydration in the TTL has been studied by comparing the observed water vapour mixing ratio (OMR) and the minimum saturation mixing ratio ( $SMR_{min}$ ) of the air parcels having been exposed to during horizontal advection.  $SMR_{min}$  has been estimated by using a bundle of isentropic backward trajectories corresponding to the air parcels observed by water vapour sondes (Hasebe et al., 2007). The OMR in the lower TTL proved to be about twice as much as  $SMR_{min}$  in the Western Tropical Pacific. The information of ice particles given by simultaneously operated lidars indicates that SVCs do exist under supersaturation up to several ten percent (Shibata et al., 2007). However, the observational data are still too limited and the accumulation of observational evidence is definitely needed to improve our understanding of the TTL dehydration.

In the present analysis, mutual relationships between OMR and  $SMR_{min}$  are further examined by updating and reexamining the data taken at Tarawa (1.4° N, 172.9° E), Biak (1.2° S, 136.1° E), Watukosek (7.6° S, 112.7° E), Bandung (6.9° S, 107.6° E), Kototabang (0.2° S, 100.3° E), Hanoi (21.0° N, 105.8° E), and San Cristóbal (0.9° S, 89.6° W) since 1998. Those data obtained by SW are not used in the present study while those by FPH and CFH are analyzed to achieve better homogeneity in the analyzed data. Those features are interpreted in terms of meteorological conditions such as local convective activity, isentropic levels, season and El Niño/Southern Oscillation (ENSO) status. Detailed interpretation of the observed water vapour amount in terms of the origin and the Lagrangian temperature history of the air parcel has also been attempted on each sounding basis as case studies. The analysis, extended by searching for the “match pairs” among sonde data to directly quantify the change in the water vapour amount along advection, requires detailed examination on the “match criteria” so that the results are not given here but are described in a separate paper by Inai et al. (2012).

Section 2 introduces the SOWER campaigns including the sounding statistics and climatological conditions. The method of analysis for water vapour sonde data and corresponding trajectories is presented in Sect. 3. The results, both on the statistical

relationships between OMR and  $SMR_{\min}$  and some detailed meteorological interpretation for a couple of cases, are described in Sect. 4. Some discussion is made on the obtained results in Sect. 5 before summarizing the findings in Sect. 6.

## 2 SOWER campaigns

SOWER water vapour observations have been conducted on a campaign basis. Those stations that have operated frostpoint hygrometers FPH and CFH are listed in Table 1. The field of campaigns has migrated from the Eastern to the Western Tropical Pacific and the time of operation has been shifted exclusively to boreal winter as our studies are becoming focused on the dehydration processes in the TTL. These years overlap with the developing period of CFH and it was not until 2005 that mostly stable data became available from it. The following analysis, therefore, starts from the development of an objective analysis scheme of sonde data that might not be homogeneous in the quality of observed values (Sect. 3).

SOWER aerosol observations have been made by Mie lidars installed at Bandung, Biak, and Kototabang in Indonesia (Shibata et al., 2007) and Tarawa in Kiribati together with that on research vessel “Mirai” (Fujiwara et al., 2009). Those data shown in the present analysis are the backscattering coefficient at the wavelength of 532 nm taken by that at Biak. See Shibata et al. (2012) for more descriptions on the Biak lidar system. Scattering from aerosol is also observed, although only two launches so far in SOWER campaigns, by balloon-born aerosol sonde named COBALD ([http://www.iac.ethz.ch/groups/peter/research/Balloon\\_soundings/COBALD\\_sensor](http://www.iac.ethz.ch/groups/peter/research/Balloon_soundings/COBALD_sensor)) developed by Frank G. Wienhold in the group of Thomas Peter at Swiss Federal Institute of Technology (ETH). The optical properties of aerosol and larger particles are measured by the backscatter ratio at the wavelengths of 455 nm and 870 nm taking the signal fraction by air molecules as reference.

Before looking into some details of the dehydration processes, it is useful to make a brief look at the averaged meteorological fields for representative campaigns. The

### TTL dehydration

F. Hasebe et al.

Title Page

Abstract

Introduction

Conclusions

References

Tables

Figures



Back

Close

Full Screen / Esc

Printer-friendly Version

Interactive Discussion



latitude-longitude distributions of the horizontal wind components (arrows) and temperature (color) on 370 K isentropic surface averaged over the campaign period are shown in Fig. 1. This isentrope has been chosen to be close to the cold point tropopause (CPT). The white circles are the location of the stations. There is obviously a clear interannual variations reflecting the ENSO condition and the phase of the quasi-biennial oscillation (QBO). The occurrence of ENSO generally shifts the western tropical cold core in the TTL to the east together with the general warming of the troposphere. The QBO modulates the zonal mean temperature as expected from the thermal wind relationship with the zonal wind (Plumb and Bell, 1982) leading to the warm (cold) TTL corresponding to the arrival of the descending westerly (easterly) at the lowermost stratosphere (Hasebe, 1994).

### 3 Method of analysis

#### 3.1 Processing of sonde data

While the atmospheric pressure  $p$  is usually used as an independent variable for radiosonde observations of temperature  $T$  and horizontal wind components, it is also subject to observational uncertainties. To minimize possible mean bias in the raw pressure data, we have employed pressure correction, usually small however, by the method proposed by Inai et al. (2009) prior to the analysis whenever the simultaneous GPS height data are available.

The mixing ratio is conveniently used for the quantitative description of tracers as it is conserved following the atmospheric motion as long as chemical production/loss and physical condensation/evaporation are negligible. The primary quantity for the water vapour measurements by chilled-mirror hygrometers (such as FPH) is the frostpoint temperature  $T_{\text{fr}}$ . It is converted to water mixing ratio  $\chi$  referring to the ambient pressure. In the present analysis, all observed values are projected on isentropic surfaces to make an advantage of the conservation of both  $\chi$  and potential temperature  $\theta$  following

## TTL dehydration

F. Hasebe et al.

Title Page

Abstract

Introduction

Conclusions

References

Tables

Figures



Back

Close

Full Screen / Esc

Printer-friendly Version

Interactive Discussion



adiabatic atmospheric motion. The data processing procedure that includes an objective evaluation of  $\chi$  and its observational uncertainties on isentropes is described in the following.

The frostpoint hygrometers maintain constant frost on a mirror by using its reflectance as a feedback signal to control the mirror temperature so that it is equal to the frostpoint temperature of the ambient air. The accuracy of the measurements depends on several aspects such as the temperature uniformity of the mirror, calibration of the thermistor and so on. The largest source of the uncertainty for CFH measurements is, however, the stability of the feedback controller resulting in the overall uncertainties of  $0.51\text{ }^{\circ}\text{C}$  in  $T_{\text{fr}}$  corresponding to the range from 4 % in the tropical lower troposphere to 10 % in the middle stratosphere in water mixing ratio (Vömel et al., 2007a). What is specific for the frostpoint hygrometer measurements is the finite length of time for the frost on the mirror to achieve equilibrium with the environment. In the lower tropospheric condition, e.g.  $20\text{ }^{\circ}\text{C}$ , the response time  $\tau$  for the instrument to maintain frost on the mirror is short enough to be neglected. However, it becomes longer higher up in the atmosphere due to lengthening of the time for vapour-water and vapour-ice equilibrium on the mirror to be achieved. It may reach 10 s and as long as 80 s under the condition of  $-30\text{ }^{\circ}\text{C}$  and  $-60\text{ }^{\circ}\text{C}$ , respectively, in the case of SW (Fujiwara et al., 2003). The CFH, on the other hand, is designed to optimize the individual settings of the on board feedback controller so that  $\tau$  be minimum without causing spurious fluctuations in the observed data (Vömel et al., 2007a,b). In the upper troposphere and lower stratosphere, however,  $\tau$  could be much longer than the sampling interval of about 7 s for TMAX-C and 1.4 s for V2C systems that transmit telemetry data to ground stations. As a result, the fluctuations shorter than  $\tau$  in the raw radiosonde data are mostly artifact created by instrumental feedback system. The circumstances are clearly seen in the early NOAA/FPH data that rely on the TMAX-C system (Fig. 2). The diagram at the top-left illustrates the ascending (green) and descending (purple) vertical profiles of water mixing ratio taken at San Cristóbal in March 1998. Some detailed structures, if any, are not resolved by relatively large uncertainties in the fluctuated data. Such instrumental

## TTL dehydration

F. Hasebe et al.

Title Page

Abstract

Introduction

Conclusions

References

Tables

Figures

◀

▶

◀

▶

Back

Close

Full Screen / Esc

Printer-friendly Version

Interactive Discussion



noise is greatly reduced in ten years thanks to the improvement in the mirror temperature control system as can be seen from those at the top-right of the figure showing the similar profile observed at Biak in January 2008 by CFH with V2C system.

Such instrumental noise could be reduced by smoothing the sequence of raw frost-point temperature profiles as long as the noise could be regarded as random. The details of data processing on pressure levels including the smoothing procedure are described in Appendix A1. The smoothing with the time interval similar to that for  $T_{fr}$  has been applied to  $p$  and  $T$ , both primary observed quantities for radiosondes, to guarantee mutual consistency among derived quantities. It should be mentioned, however, that the response time for  $p$  and  $T$  is much shorter than the sampling intervals in all observation range. Then the estimated uncertainties in  $p$  and  $T$  are mostly composed of natural variability rather than instrumental noise. The details of the estimation of uncertainties in the smoothed values are also given in Appendix A1.

We now have the smoothed values of pressure  $\bar{p}_i$ , temperature  $\bar{T}(\bar{p}_i)$ , and frostpoint temperature  $\bar{T}_{fr}(\bar{p}_i)$ , together with the estimates of errors  $\Delta p(\bar{p}_i)$ ,  $\Delta T(\bar{p}_i)$ , and  $\Delta T_{fr}(\bar{p}_i)$ , respectively, for each sounding level  $i$ . The partial pressure of water is given by the saturation water pressure  $e_{sat}$  corresponding to  $\bar{T}_{fr}$ . Goff-Gratch equation (Goff and Gratch, 1946; Murray, 1967; Murphy and Koop, 2005; Hasebe et al., 2007) is used for its estimation. The water mixing ratio  $\chi(\bar{p}_i)$  is readily derived by dividing  $e_{sat}$  by  $\bar{p}_i$ . Before projecting  $\chi(\bar{p}_i)$  on isentropes, we estimate the errors in  $\theta(\bar{p}_i)$  as well as  $\chi(\bar{p}_i)$ . The detailed procedure is given in Appendix A1. All these quantities are taken into account in deriving the uncertainties of water mixing ratio on isentropes. The procedure on the projection of the pressure-based values on isentropes is described in Appendix A2. The results are shown in the middle of Fig. 2. The horizontal bars indicate the range of uncertainties that arise from total (both instrumental and natural) variabilities. Due to the mutual dependency of errors among those data used in the smoothing, it is not appropriate to identify any specific value for the probability that the population mean sits within the range of these bars (see Appendix A1). However, it does provide useful information on the range of uncertainties in the obtained profiles.

## TTL dehydration

F. Hasebe et al.

Title Page

Abstract

Introduction

Conclusions

References

Tables

Figures

◀

▶

◀

▶

Back

Close

Full Screen / Esc

Printer-friendly Version

Interactive Discussion



## TTL dehydration

F. Hasebe et al.

[Title Page](#)[Abstract](#)[Introduction](#)[Conclusions](#)[References](#)[Tables](#)[Figures](#)[◀](#)[▶](#)[◀](#)[▶](#)[Back](#)[Close](#)[Full Screen / Esc](#)[Printer-friendly Version](#)[Interactive Discussion](#)

Some differences between the ascending (green) and descending (purple) profiles are noticed in the range between 350 and 420 K from the Biak data (Fig. 2 middle right) exhibiting a wavy structure with maxima and minima located at higher (lower) isentrope in the ascending (descending) data. They are mostly attributable to the delay in the response of the frost on the mirror of the hygrometer rather than the difference in the sampled air volume. Full understanding of such behavior requires adequate knowledge of the mirror temperature control system. In the present analysis, we make a practical approach by applying an inverse filtering to the observed data to compensate for the phase delay as much as possible. The method of phase correction is described in Appendix A3. The adopted values of the response time  $\tau$  are 4 s in the upper troposphere ( $250 > p \geq 150$  hPa), 8 s in the lower TTL ( $150 > p \geq 120$  hPa), and 10 s in the upper TTL and the stratosphere ( $p < 120$  hPa) while the lag is neglected ( $\tau = 0$ ) in the lower- and middle troposphere ( $p \geq 250$  hPa). The corrected profiles are shown at the bottom of Fig. 2. Unfortunately the sharp minimum in the ascending data near 370 K cannot be reproduced from the descending data as the instrument does not at all capture the signal during descent. However, we could see the phase correction working reasonably well to compensate for the phase lag inevitable from the observational principle of the frostpoint hygrometer. This correction makes us more confident in the degree of supersaturation derived from the analysis (Sect. 4).

### 3.2 Trajectory analysis

The water content of any air parcel observed by sondes is controlled by many factors such as the dehydration it has experienced during horizontal advection and hydration due to evaporation of cloud particles and/or precipitation from above in addition to the amount of water it originally contained. The degree of dehydration subject to observed air parcels is examined by using the temperature history along the trajectories. For this purpose, isentropic backward trajectories are calculated referring to the global analysis field.

**TTL dehydration**

F. Hasebe et al.

[Title Page](#)[Abstract](#)[Introduction](#)[Conclusions](#)[References](#)[Tables](#)[Figures](#)[◀](#)[▶](#)[◀](#)[▶](#)[Back](#)[Close](#)[Full Screen / Esc](#)[Printer-friendly Version](#)[Interactive Discussion](#)

We employ  $1.125^\circ$  latitude by  $1.125^\circ$  longitude horizontal resolution and 60 model-level (L60) version of ECMWF reanalyses ERA40 in six-hour interval until December 2002. After that time, the dataset has been switched to  $1^\circ$  by  $1^\circ$  six-hour interval ECMWF operational analysis in L60 till January 2006 and in L91 thereafter. Because of the limited spatio-temporal resolution of the model, the trajectory calculations based on the global analysis field cannot get rid of certain amount of errors arising from small scale features unresolved in the model. Although any complete assessment of the accuracy of the derived trajectories is practically impossible, some comparisons of our sonde data with the global analysis field will be helpful to get some idea on the limitation of such calculations. Before calculating the trajectories, therefore, a brief survey is conducted by comparing the vertical profiles of temperature and wind components provided by ECMWF analysis field against our sonde observations.

Figure 3 shows an example from such comparisons. The sequences of crosses that look like heavy lines are the sonde profiles of temperature (black) and zonal (red) and meridional (blue) wind components, while sparsely plotted diamonds are those interpolated to the station at the time of launch from the six-hour interval ECMWF gridpoint data (left). ECMWF data on model levels are interpolated to prescribed pressure levels with adequate interval so as not to lose model's vertical resolution. The sonde data are projected on potential temperature surfaces in every 0.2 K between 340 and 360 K, 0.5 K between 360 and 380 K, and every Kelvin from 380 to 700 K. The results are shown on the right where sonde data are illustrated in crosses while the ECMWF data converted from pressure coordinates are shown in diamonds. As is expected, small scale features in sonde data are missing in the interpolated ECMWF data even though the overall features agree reasonably well between the two datasets.

Statistical features derived from such comparisons between sonde and ECMWF fields are illustrated in Fig. 4, that shows the mean bias of the analysis field against sonde data at SOWER stations superposed by bars corresponding to the confidence interval of 99%. The top and bottom panels are drawn by using the data before and after December 2006, respectively, when the operational use of GPS temperature data

**TTL dehydration**

F. Hasebe et al.

[Title Page](#)[Abstract](#)[Introduction](#)[Conclusions](#)[References](#)[Tables](#)[Figures](#)[◀](#)[▶](#)[◀](#)[▶](#)[Back](#)[Close](#)[Full Screen / Esc](#)[Printer-friendly Version](#)[Interactive Discussion](#)

by COSMIC started in ECMWF. There found some noticeable biases especially in zonal wind (center; red). It is interesting to note that the biases are reduced in the statistics after December 2006 (bottom) not only in temperature but also in wind components. The improvement in the quality of meteorological fields in general may indicate model's response to the high resolution COSMIC temperature data adjusting the dynamical fields being consistent with observed temperature.

Figure 5 shows another type of comparison that illustrates time series of temperature (black) and zonal (red) and meridional (blue) wind components on 370 K isentrope at Biak covering the 2006 (top) and 2007 (bottom) campaigns in January. The overall agreement is good in the latter while some noticeable differences are found in the former. Although it is hard to draw generalized conclusion from our limited comparisons, it is quite impressive to see the improvement of the ECMWF analysis in the COSMIC era.

In spite of such shortcomings inevitable in the analysis field, trajectory calculations have proved to be a convenient tool in many purposes including the dehydration studies. To cope with the uncertainties and to try to deduce as much information as possible, we will make probabilistic approach throughout our study. The advected air parcel is expressed by a set of segments initialized in the area representative of the air mass observed by sondes. This will help visualize the deformation of the air parcels due to wind shear and the bifurcation of the trajectories at the saddle point encountered along the advection (e.g. Hasebe et al., 2007, Fig. 1). Figure 6 illustrates the distribution of such segments on initialization (equally spaced crosses filling the circle over the station with the density of 10 segments per degree) superposed on three sonde flight tracks (solid lines in color). The diameter of the circle has been chosen to 1° in latitude/longitude to cover almost entire flight tracks of typical sonde flights intending to cover the range of uncertainties in the location of the observed air mass. The temperature history of each air mass observed by sondes is examined by using a bundle of trajectories initialized at these points.

## TTL dehydration

F. Hasebe et al.

[Title Page](#)[Abstract](#)[Introduction](#)[Conclusions](#)[References](#)[Tables](#)[Figures](#)[◀](#)[▶](#)[◀](#)[▶](#)[Back](#)[Close](#)[Full Screen / Esc](#)[Printer-friendly Version](#)[Interactive Discussion](#)

An example from such trajectories is shown in Fig. 7, which shows the horizontal projection of seven-day backward trajectories on 353 K isentrope corresponding to the sonde flight from Biak on 8 January 2006. Those on the top panel are color-coded by the saturation mixing ratio (SMR) for the advected air parcel estimated from ECMWF analysis filed. We can see that the air parcel was exposed to the condition with relatively high SMR about 3–4 days prior to observation as indicated by orange portion of the trajectories while it experienced low SMR at the early and final stages of the advection as judged by light green. Possible influence of penetrating deep convection on the advected air parcel is examined by comparing instantaneous air temperature  $T$  given by the analysis field with underlying earth's equivalent blackbody temperature  $T_{bb}$  observed by geostationary meteorological satellites. The resolution of  $T_{bb}$  is 20 pixels per degree (i.e. roughly  $5 \times 5$  km) with one hour time interval. The results are shown on the bottom panel of the figure that shows the trajectories color coded by the difference between  $T_{bb}$  and  $T$ . The dark colors in purple indicate that the difference between the two ( $T_{bb} - T$ ) is negative meaning that the cloud top is colder and thus higher than the advected air parcel. The southern portion of the trajectories, therefore, indicates that the air parcel may have encountered deep convection and that the air mass may have been replaced by convectively lifted lower-tropospheric humid air during the early stage of advection. This kind of information will be used in the interpretation on the water content of the air mass observed by hygrometers.

## 4 Results

### 4.1 Case study from individual soundings

In this subsection, two selected profiles are discussed in detail with the aim of providing a meteorological interpretation of the overall results in terms of TTL dehydration. The left hand panel of Fig. 8 shows the vertical profiles of temperature ( $T$ ; black), frostpoint temperature ( $T_{fr}$ ; green), and ozone mixing ratio ( $O_3$ ; purple) observed on 11 January

## TTL dehydration

F. Hasebe et al.

[Title Page](#)[Abstract](#)[Introduction](#)[Conclusions](#)[References](#)[Tables](#)[Figures](#)[◀](#)[▶](#)[◀](#)[▶](#)[Back](#)[Close](#)[Full Screen / Esc](#)[Printer-friendly Version](#)[Interactive Discussion](#)

2008 at Biak. The atmosphere below 354 K potential temperature is under near saturation as seen from the almost overlapped profiles of  $T$  and  $T_{fr}$ . Similarly, the air between 363 and 368 K is close to saturation ( $RH_{ice} > 70\%$ ). The layer between 355 and 363 K, sandwiched by humid regions, is almost isothermal and exhibits little change in  $T_{fr}$  as well. The fact that  $T_{fr}$  is appreciably smaller than  $T$  indicates the dryness of this layer, as can be seen from the right panel of Fig. 8, where the corresponding profiles of water mixing ratio (green) and relative humidity with respect to ice ( $RH_{ice}$ ; red) show low values; those of  $RH_{ice}$  stay within the range between 25 and 50 % in this layer in contrast to the near saturation below and above. No ice particle has been detected by the COBALD Backscatter Sonde in this dry layer as can be seen from the profile of the backscattering ratio (BSR; blue).

In the saturated layer below 354 K, COBALD shows a pronounced cirrus layer, with a geometric thickness of about 2 km and an estimated optical thickness of about 0.1. Although the uncertainties of  $RH_{ice}$  in this layer are relatively large, the maximum value within the particle layer reaches  $129 \pm 14\%$ , i.e. clearly supersaturated. This cloud layer is also detected from the lidar at Biak station. Figure 9 shows the time-height section of the backscattering coefficient at 532 nm observed by lidar. We can see clouds at the altitude range from 12 to 16 km illustrated in warm colors. The large values of the depolarization ratio (not shown) simultaneously observed with backscattering coefficient indicate that the cloud particles are frozen to ice (cirrus clouds).

It is interesting to investigate the meteorological foundation of this layered structure from a Lagrangian point of view. We can see that the profile shown in Fig. 8 is directly related to the atmospheric flow pattern and the region from which the air masses originated. Figure 10 illustrates the horizontal projection of the isentropic backward trajectories color-coded by the instantaneous saturation mixing ratio (SMR) on 370 (upper humid layer), 360 (middle dry layer) and 353 K (in the midst of the saturated layer) surfaces for the sonde profile shown in Fig. 8. The SMR for these air masses commonly shows relatively high values while they traveled in midlatitude but it becomes low after they reached equatorial region within  $\pm 10$  degrees latitude, where they were exposed

to low temperature. This is due to the general tendency of the latitudinal inclination of isentropes. However, we can readily see the clear difference of the 360 K air masses against those on 353 and 370 K surfaces: those on 360 K originated from the northern midlatitudes while those on both 353 and 370 K have been advected from the southern midlatitudes. The gross features of the vertical structure are thus related to the origin of the air masses on the hemispheric scale.

If we look into more details of the SMR along trajectories, we can see that the air parcels have experienced a couple of cold events. For example, those on 370 K were advected in an extremely cold region far east of Papua New Guinea with the SMR as low as 0.5 ppmv (182.4 K on 169.1 hPa), which is much lower than the observed mixing ratio (OMR) of  $1.7 \pm 0.2$  ppmv over Biak. The difference between OMR and SMR is a measure of the dehydration efficiency observationally deduced. Similar calculation for the air parcel on 360 K shows that the minimum SMR during the seven days ( $SMR_{\min}$ ) is about 1.4 ppmv (185 K, 99 hPa) as compared to the OMR of  $2.9 \pm 0.4$  ppmv, and  $SMR_{\min} = 5.4$  ppmv (196 K, 160 hPa) against  $OMR = 9.8 \pm 1.7$  ppmv for 353 K. What is specific for those on 353 K is that those parcels over Biak are just experiencing low temperature (197.6 K) comparable to that of  $SMR_{\min}$ , being consistent with the existence of ice particles confirmed by COBALD and lidar.

In order to examine possible intrusion of deep convection into the advected air masses, Fig. 11 compares the SMR along the trajectories with the underlying equivalent blackbody temperature ( $T_{bb}$ ). The top panel is the same as the bottom of Fig. 10 but drawn only for three days before sonde observation, while the bottom is the same as the top except that the trajectories are color-coded by the difference of the instantaneous  $T_{bb}$  from air temperature  $T$ . The air parcels experienced relatively cold environment for four times during the three days; just over Biak, about a half day, about 45 h, and about 65 h before arrival at Biak. Between these events, they passed relatively warm environment, which means that they were advected at relatively high pressure (low altitudes). The last of such events is found when they passed  $140^\circ$  E. Between this event and the arrival over Biak, 5 to 11 GMT on 11 January 2008, some portion of them

## TTL dehydration

F. Hasebe et al.

Title Page

Abstract

Introduction

Conclusions

References

Tables

Figures

◀

▶

◀

▶

Back

Close

Full Screen / Esc

Printer-friendly Version

Interactive Discussion



## TTL dehydration

F. Hasebe et al.

Title Page

Abstract

Introduction

Conclusions

References

Tables

Figures

◀

▶

◀

▶

Back

Close

Full Screen / Esc

Printer-friendly Version

Interactive Discussion



may have encountered deep convection as the values less than 20 K are observed for  $T_{bb} - T$ . It is hard to identify the critical value of  $T_{bb} - T$  for which deep convection actually reaches air parcels drifting above, but the minimum value of 14 K recognized in this case may be low enough to suspect possible intrusion of deep convection. The saturation around 353 K over Biak (Fig. 8) is thus inferred from possible intrusion of deep convection within several hours before sonde observations. There have been no such events ( $T_{bb} - T \leq 20$  K) for the trajectory sets on 360 and 370 K.

Another sounding shown in Fig. 12 exhibits very humid layers in terms of relative humidity. One is the thin layer centered at 351 K and the other is the broad region (in isentropic coordinates) around the cold-point tropopause (CPT) near 380 K. The former is not discussed here as the behavior of the instrument raises questions on the validity of the obtained values. In the latter case around 380 K, the layer of supersaturation spans from 374.0 K (17 551 m) to 402.0 K (18 720 m) in potential temperature with the maximum  $RH_{ice}$  value reaching  $179 \pm 14$  % on 378.5 K (18 247 m). The atmospheric temperature on this level is 180.2 K ( $-93.0^\circ\text{C}$ ), which is slightly higher than that of the CPT of 179.8 K ( $-93.3^\circ\text{C}$ ) found in the raw sonde record on 379.5 K (18 334 m). This supersaturation is found within the cirrus clouds as can be seen from the lidar backscatter signal (Fig. 13). The  $RH_{ice}$  value of  $179 \pm 14$  % within the cirrus is extremely high and much higher than those reported previously (Krämer et al., 2009). As expected, the subsaturated layer at around 369.0 K (16 982 m) with the  $RH_{ice}$  value of  $96 \pm 10$  % shows no signal in the cross section of the lidar backscattering coefficient. The cirrus clouds appearing moments after the sonde passage at a little lower than 14 km in lidar data do not exhibit appreciable signal in sonde humidity profile, although a small maximum of  $80 \pm 5$  % in  $RH_{ice}$  is seen at this altitude. Taking these measurements at face value with the assumption that the air masses sampled by sonde and lidar are identical, a sudden cooling due to a temperature perturbation of at least 2 to 6 K would be required to explain the cloud development in terms of heterogeneous or homogeneous nucleation, respectively. The depolarization ratio (not shown) indicates all these cirrus layers consist of ice particles. The isentropic back trajectories for 370 to 380 K

levels (not shown) are traced back to the east suggesting possible moistening by deep convection even at 380 K level.

## 4.2 Statistical description of the dehydration

We have seen that the simultaneous observations of water vapour and ice particles by hygrometers and lidar/COBALD sonde, respectively, are extremely useful to describe the existence or the lack of condensed matter in highly supersaturated regions. We have also seen that the humidity profiles reflect in some cases the difference in the origin of the air mass. In addition to the close look at individual profiles as has been done above, we will now investigate general features of TTL dehydration as retrieved from our current observation network.

Figure 14 is an extended version of Fig. 7 of Hasebe et al. (2007) providing scatter diagrams of OMR against  $SMR_{\min}$  for six different isentropic levels. Symbols specify season while colors refer to observation station(s). The search for the values  $SMR_{\min}$  has been limited to seven-day backward trajectories. Special attention is paid to possible impacts of deep convection, which may not only violate the assumed adiabatic motion in using isentropic trajectories but also cause the loss of identity of the air parcel. In case the intrusion of deep convection is suspected,  $SMR_{\min}$  has been sought from those portions of trajectories after such events. The intrusion is assumed to be subject to the condition  $T_{bb} - T \leq 12$  K, referring to the investigation of Inai et al. (2012). Large error bars in OMR mostly reflect uncertainties of NOAA/FPH and CFH in their early development stages. The basic interpretation of the scatter diagrams is summarized in the following; detailed features noticeable for each isetrope are described in Appendix B.

OMR- $SMR_{\min}$  pairs that fall onto the diagonal line (solid line) are likely due to a dehydration event during the 7 days upstream, which depleted the gas phase to the saturation value and subsequently conserved the mixing ratio. However, as nucleation of ice requires a supersaturation (e.g. 60% for homogeneous nucleation of ice, see Koop et al., 2000), the OMR might be up to a factor of 1.6 higher than  $SMR_{\min}$  without

### TTL dehydration

F. Hasebe et al.

Title Page

Abstract

Introduction

Conclusions

References

Tables

Figures

◀

▶

◀

▶

Back

Close

Full Screen / Esc

Printer-friendly Version

Interactive Discussion



## TTL dehydration

F. Hasebe et al.

[Title Page](#)[Abstract](#)[Introduction](#)[Conclusions](#)[References](#)[Tables](#)[Figures](#)[◀](#)[▶](#)[◀](#)[▶](#)[Back](#)[Close](#)[Full Screen / Esc](#)[Printer-friendly Version](#)[Interactive Discussion](#)

leading to dehydration. The points between the solid and dashed lines, corresponding to saturation and 60 % super saturation, respectively, might be of this nature. Some finite length of time needed to complete dehydration after initiation of ice formation is another factor that lead to  $OMR > SMR_{min}$ . Furthermore, lower levels might experience increases in OMR due to sedimenting ice particles, which fall in from higher levels and evaporate at the level of interest. Those points with the OMR far exceeds  $1.6 \times SMR_{min}$  found at  $\theta = 360$  and  $365$  K may well be interpreted by this sedimentation effect.

Pronounced occurrence of  $OMR < SMR_{min}$  is found above and below the TTL, i.e. in the stratosphere ( $\theta = 400$  K) and middle troposphere ( $\theta = 350$  K). At  $\theta = 400$  K, which is located above the level of net zero clear-sky radiative heating (LZRH, i.e. where radiative heating and cooling balance each other, located at 125 hPa or about 15.5 km or 360 K potential temperature), see Fueglistaler et al. (2009), air has ascended diabatically into warmer regions and the last dehydration event close to the cold point tropopause is longer ago than the 7-day span of the trajectories. As a consequence, besides a few exceptions, these parcels are much drier than  $SMR_{min}$ . At  $\theta = 350$  K (around 13 km), on the other hand, the diabatic motion outside the convective system is downward compensating for net radiative cooling. As the tropical convective motions frequently reach 350 K (Atticks and Robinson, 1983), the air masses sampled by radiosondes are often those flowed out from convective systems. The water content for such air masses is mostly determined by the temperature of the outflow level (e.g.  $-60$  °C), leading to the near correspondence between OMR and  $SMR_{min}$  with the factor one order of magnitude larger than that of the upper TTL. The displacement down from the diagonal line will result from the radiatively driven descent that takes place after precipitation and/or evaporation of condensed particles. The diagonal alinement of stations from Tarawa (TR; upper right) to Hanoi (HN; lower left) would be also understood in terms of the outflow temperature. The scatter diagrams derived from the SOWER chilled-mirror hygrometer network data in the Tropical Pacific thus show a wealth of intricate facets for the different stations and seasons, which are detailed in Appendix B.

## 5 Discussion

Radiosonde observations of water vapour and ozone over the Tropical Pacific conducted during SOWER campaigns are used to analyze the efficiency of the cold-trap dehydration taking place in the air parcels advected horizontally in the TTL. Chilled-mirror hygrometers such as FPH and CFH are used to obtain water vapour mixing ratio suitable for observing the extreme dryness in the tropical upper troposphere, TTL and the lower stratosphere. The estimates of the uncertainties are derived, together with an attempt of correcting the phase delay in the frostpoint temperature measurements, to improve our confidence in the degree of supersaturation. The response time given in this procedure has been empirically determined as a function of atmospheric pressure so that the ascending and descending profiles agree between each other. The stratospheric value adopted in the present study (Table 2) is a little larger than that shown by Vömel et al. (2007b) obtained by comparisons with fast-response fluorescence sensors. The sole values used throughout the analysis period have been determined by CFH observations and may not be appropriate for those data obtained from early campaigns as the instrument has been continuously upgraded. The sequence of processing described above, even if incomplete, helps the present analysis to gain the credibility of the results.

Trajectory analyses presented in this paper depend on the global analysis field. These days growing numbers of global analyses are emerging. There are differences among them (e.g. Liu et al., 2010; Schoeberl and Dessler, 2011) and our use of high-resolution model-level ECMWF global analysis is only one of possible choices. In this sense, it may be hard to generalize our current results. One of the possible ways to cope with this problem will be to conduct multi-model comparison such as being done among climate models by the climate change research community. Systematic comparison among major global analysis fields (Fujiwara et al., 2012) including that of the TTL trajectories will be an important step awaiting to be done for the task of our community. Another vector to attain more confidence in the results will be the use of

### TTL dehydration

F. Hasebe et al.

Title Page

Abstract

Introduction

Conclusions

References

Tables

Figures

◀

▶

◀

▶

Back

Close

Full Screen / Esc

Printer-friendly Version

Interactive Discussion



data assimilation technique incorporating the observed data in the analysis field. Our preliminary analysis indicates that the improved time resolution in particular in the assimilation field will make the estimates of  $SMR_{min}$  more realistic.

The supersaturation as large as  $179 \pm 14\%$  of the relative humidity with respect to ice ( $RH_{ice}$ ) has been observed around the cold point tropopause. This value is one of the highest among those observed in the cirrus clouds and might compare only with those found by Popp et al. (2007) who discussed such high supersaturation with the presence of condensed-phase nitric acid. Unfortunately, the estimates of uncertainty shown above does not correspond to well-defined confidence interval of any kinds because of the mutual dependence of errors in profile data (Appendix A1). Therefore, our results may be regarded as close to or within the limit of the homogeneous freezing threshold of Koop et al. (2000). Since such occurrences are rather limited in our observations, more observational evidence is apparently needed to estimate possible upper limit of supersaturation in the TTL. For this purpose, it is preferable to launch aerosol sensors such as optical particle counters on board radiosonde (e.g. Iwasaki et al., 2007) since an extremely low concentration of aerosol, below the detection limit of lidars, might be critically important.

The progress of dehydration for the air parcels advected in the TTL is examined by comparing the  $SMR_{min}$ –OMR scatter plots among isentropes. Gradual removal of water associated with the air parcels' slow ascent in the TTL is reflected to the manner how the OMR and the corresponding  $SMR_{min}$  are distributed on the plane. The near alignment along the diagonal line on 350 K has been interpreted as an indication of minor role of horizontal advection on controlling the water content on this isentrope. This is consistent with the notion by Selkirk et al. (2010) that water variability below 350 K is decoupled by such processes but more related to convective cloud activity. On the other hand, the distribution of the plots is not symmetric with respect to the diagonal but is found to be distributed unevenly to the upper left on the isentropes 360, 365 and 370 K. This is consistent with the findings by Schiller et al. (2009) in which the aircraft observations of water vapour show values larger than  $SMR_{min}$  below 380 K

## TTL dehydration

F. Hasebe et al.

Title Page

Abstract

Introduction

Conclusions

References

Tables

Figures

◀

▶

◀

▶

Back

Close

Full Screen / Esc

Printer-friendly Version

Interactive Discussion



## TTL dehydration

F. Hasebe et al.

Title Page

Abstract

Introduction

Conclusions

References

Tables

Figures

◀

▶

◀

▶

Back

Close

Full Screen / Esc

Printer-friendly Version

Interactive Discussion



isentropes. They attributed this difference as the recent moistening of the advected air parcels by deep convection. Our interpretation, however, has been to put much emphasis on the progress of the cold-trap dehydration during the horizontal advection accompanied by the gradual ascent in the TTL, because such uneven distributions are not found on 350 K where the moistening by deep convection is much more frequent than those isentropes above. The diagonal alignment of the  $SMR_{\min}$ –OMR scatter plots on 380 K and the increase of OMR from 380 K to 400 K isentropes are indications that the dehydration is almost complete on 380 K. However, the detailed processes how this entry value is modulated to form stratospheric values are not well understood. Our notion on some role of hydration processes (Appendix B) is preliminary and needs to be revisited by the studies based on the observed data that cover the whole season over the entire tropics.

In the Lagrangian description of the horizontal advection, possible penetration of convective clouds and a subsequent loss of air parcel's identity is always a matter of concern. In the present analysis, cumulus penetration has been diagnosed by comparing the temperature of advected air parcel  $T$  with the equivalent blackbody temperature  $T_{bb}$  of the underlying atmosphere, and once the condition  $T_{bb} - T \leq 12$  K is met, the value  $SMR_{\min}$  has been sought from those portions of trajectories only after such events. At this moment, there is no definite reasoning for the choice of the critical value 12 K (see Sect. 3 of Inai et al., 2012). Fortunately, however, the obtained results shown in Fig. 14 do not essentially change with the choice of this critical value. The use of a new method proposed by Hamada and Nishi (2010) could be an alternative, although some of our stations are outside the coverage of the Japanese geostationary satellite, Multifunctional Transport Satellite (MTSAT), necessary for applying their algorithm.

Selkirk et al. (2010) introduced tropopause saturation layer (TSL) whose top was defined by the highest altitude of saturation while the bottom was the altitude of the minimum in the water mixing ratio found below the TSL top. They argued that the water mixing ratio at the cold point tropopause (CPT) often represented that in the stratosphere since the CPT was sometimes created by adiabatic cooling associated

## TTL dehydration

F. Hasebe et al.

[Title Page](#)[Abstract](#)[Introduction](#)[Conclusions](#)[References](#)[Tables](#)[Figures](#)[◀](#)[▶](#)[◀](#)[▶](#)[Back](#)[Close](#)[Full Screen / Esc](#)[Printer-friendly Version](#)[Interactive Discussion](#)

with the upward displacement due to atmospheric waves and that the stratospheric entry value of water was effectively determined by the minimum water mixing ratio in the TSL. This argument is based on two observation campaigns conducted in the Eastern Tropical Pacific (Costa Rica) during northern summer, in which the top of TSL were 380 and 381 K and the average minima in the TSL water were 5.2 and 4.8 ppmv, respectively. Our observations in the Western Tropical Pacific during northern winter, on the other hand, sometimes encountered supersaturation above 380 K as was shown in Fig. 12. In this case, the minimum water mixing ratio found in the TSL is 1.27 ppmv on 379.5 and 380.0 K isentropes in the processed data, while there is little indication of gravity wave disturbances. Such a low value in this particular case must be too low as to be regarded as the stratospheric entry value of water.

Possible role of Kelvin waves on the dehydration for the atmosphere being exchanged between the troposphere and the stratosphere was pointed out first by Fujiwara et al. (2001). Eguchi and Shiotani (2004) discussed the importance of the temperature and flow variations associated with the structure of the coupled Kelvin-Rossby waves in the TTL dehydration. Fujiwara et al. (2009) pointed out that the dynamical processes accompanied by the Kelvin waves are important to control cirrus formation in the TTL. It is thus quite interesting to see if the large scale wave activities might change the progress of dehydration shown in the  $SMR_{min}$ –OMR scatter plot (Fig. 14) by sorting the spatio-temporal position of the air parcels in the phase diagram of Kelvin waves, which is left for future studies.

One of the goals of our study to explore the efficiency of cold-trap dehydration is to quantify the amount of water having been removed during the horizontal advection. For this purpose, Lagrangian approach following the advected air parcels will be preferable. That is, by comparing the water amount of a specific air parcel taken by twice or more sequential observations, we could explicitly estimate the water budget for the parcel. The water vapour match, similar to those applied to the ozone depletion in the polar vortex, is being attempted by using the SOWER dataset. Since detailed examination of

the “match condition” is needed, the results are not presented here but are described in the companion paper by Inai et al. (2012).

## 6 Concluding remarks

Balloon-borne radiosonde data obtained by the chilled-mirror hygrometers and the electrochemical concentration cell ozone sondes have been analyzed for the study of the cold-trap dehydration in the Tropical Tropopause Layer (TTL). Every possible effort has been made to estimate the uncertainty of the results for the analysis being made on isentropes. Efforts are also made to adjust inevitable phase delay in the frostpoint temperature observed by hygrometers. Statistical uncertainties are sought as well in the Lagrangian description of advected air masses by using a bundle of trajectories initialized at the region surrounding the ground station.

The results are shown in individual soundings and in statistical features characterizing the TTL dehydration. Simultaneous observations of gas and liquid/solid phase water by hygrometers and lidar/COBALD sondes, respectively, prove to be useful to describe the efficiency of dehydration in terms of the relative humidity with respect to ice ( $RH_{ice}$ ). Extremely high values of  $RH_{ice}$  have been encountered reaching almost 180% within cirrus clouds at the vicinity of the cold point tropopause. For the confirmation of such findings, further accumulation of observational evidence is obviously needed. The progress of dehydration associated with the cross-isentropic slow ascent could be seen from the differences among isentropes in the scatter plots between the observed mixing ratio and the minimum saturation mixing ratio along the back trajectories associated with the observed air mass. Gross features suggest that the cold-trap dehydration is under progress on the isentropes above 360 K and reaching the final stage at around 380 K. Some moistening is also taking place before the air parcel reaches 400 K where no more dehydration could be expected.

### TTL dehydration

F. Hasebe et al.

Title Page

Abstract

Introduction

Conclusions

References

Tables

Figures

◀

▶

◀

▶

Back

Close

Full Screen / Esc

Printer-friendly Version

Interactive Discussion



## Appendix A

### Detailed procedure applied to sonde data

#### A1 Processing on sounding pressure levels

##### A1.1 Smoothing of raw sonde data

- 5 The detailed smoothing procedure intended to reduce instrumental noise of the frostpoint hygrometers is described in this subsection. Let denote the smoothed profiles of the frostpoint temperature as  $\bar{T}_{\text{fr}i}$  ( $i = 1, 2, \dots$ ):

$$\bar{T}_{\text{fr}i} = \frac{1}{2N+1} \sum_{j=-N}^N \hat{T}_{\text{fr}(i+j)}, \quad (\text{A1})$$

- 10 where  $\hat{T}_{\text{fr}(i+j)}$  refers to observed frostpoint temperature at  $(i+j)$ th data point. The confidence interval for the true frostpoint temperature,  $T_{\text{fr}i}$ , is estimated from the variance of the residue,  $\hat{T}_{\text{fr}i} - \bar{T}_{\text{fr}i}$ , with the aid of  $t$ -distribution applicable to samples from unknown population variance:

$$\bar{T}_{\text{fr}i} - \Delta T_{\text{fr}i} \leq T_{\text{fr}i} \leq \bar{T}_{\text{fr}i} + \Delta T_{\text{fr}i}, \quad \Delta T_{\text{fr}i} \equiv \frac{s_i \times t(f, \alpha)}{\sqrt{2N+1}}, \quad (\text{A2})$$

15 where  $t(f, \alpha)$  is the  $t$ -value corresponding to the degree of freedom  $f (= 2N)$  with the confidence level  $100(1 - 2\alpha) \%$ , and  $s_i$  is the sample standard deviation defined by the root-mean-square differences of the observed values,  $\hat{T}_{\text{fr}i}$ , from smoothed profile,  $\bar{T}_{\text{fr}i}$ :

$$s_i = \left\{ \frac{1}{2N} \sum_{j=-N}^N \left( \hat{T}_{\text{fr}(i+j)} - \bar{T}_{\text{fr}(i+j)} \right)^2 \right\}^{\frac{1}{2}}. \quad (\text{A3})$$

20

Title Page

Abstract

Introduction

Conclusions

References

Tables

Figures

◀

▶

◀

▶

Back

Close

Full Screen / Esc

Printer-friendly Version

Interactive Discussion



## TTL dehydration

F. Hasebe et al.

Title Page

Abstract

Introduction

Conclusions

References

Tables

Figures

◀

▶

◀

▶

Back

Close

Full Screen / Esc

Printer-friendly Version

Interactive Discussion



The smoothing interval  $2N + 1$  is determined by considering the response time empirically determined as discussed later in Appendix A3.  $\alpha$  is taken to be 0.005 in this study leading to 99 % confidence interval (Table 2). It should be noted, however, that the confidence interval thus derived must not be interpreted as it is, since the set of  $2N + 1$  data points taken along the sequential sonde data cannot be regarded as independent samples from a single population; the characteristics of air mass could change during the sonde ascent while independency among data samples is lost by the overlap due to smoothing. Actually those values of  $\Delta T_{\text{fr}i}$  obtained for CFH are often much smaller than those uncertainties deduced by Vömel et al. (2007a). For the purpose of providing practical measure of the observational uncertainties, we have added  $0.5^\circ\text{C}$  to the values of  $\Delta T_{\text{fr}i}$  estimated by Eq. (A2) for use throughout this work.

### A1.2 Estimates of errors in potential temperature and water mixing ratio

Let denote the definition of potential temperature and the Goff-Gratch equation as functions  $F$  and  $G$ , respectively. For simplicity, suffix  $i$  is omitted in the following equations:

$$\bar{\theta}(\bar{p}) \equiv F(\bar{p}, \bar{T}), \quad \bar{\chi}(\bar{p}) \equiv \frac{\bar{e}_{\text{sat}}}{\bar{p}} = \frac{G(\bar{T}_{\text{fr}})}{\bar{p}}, \quad (\text{A4})$$

on the sounding pressure level  $\bar{p}$ . By applying the law of propagation of errors, we have the estimates of errors in potential temperature and water mixing ratio as follows:

$$\Delta\theta(\bar{p}) = \left\{ \left( \frac{\partial F}{\partial \bar{p}} \Delta p \right)^2 + \left( \frac{\partial F}{\partial \bar{T}} \Delta T \right)^2 \right\}^{\frac{1}{2}}, \quad (\text{A5})$$

$$\Delta\chi(\bar{p}) = \left\{ \left( \frac{1}{\bar{p}} \frac{\partial G}{\partial \bar{T}_{\text{fr}}} \Delta T_{\text{fr}} \right)^2 + \left( \frac{G}{\bar{p}^2} \Delta p \right)^2 \right\}^{\frac{1}{2}}. \quad (\text{A6})$$

## A2 Projection of sonde data on isentropes

The water mixing ratio and its estimates of errors on an isentropic level  $\theta$  are derived by linear interpolation using values on adjacent sounding pressure levels  $\bar{p}_i$  and  $\bar{p}_{i+1}$ :

$$\bar{\chi}(\theta) = \frac{m \times \bar{\chi}_0 + n \times \bar{\chi}_1}{m + n}, \quad (\text{A7})$$

$$\begin{aligned} \Delta\chi(\theta) &= \left[ \sum_{k=0}^1 \left\{ \left( \frac{\partial \bar{\chi}(\theta)}{\partial \bar{\chi}_k} \Delta\chi_k \right)^2 + \left( \frac{\partial \bar{\chi}(\theta)}{\partial \bar{\theta}_k} \Delta\theta_k \right)^2 \right\} \right]^{\frac{1}{2}} \\ &= \frac{1}{m+n} \left[ (m\Delta\chi_0)^2 + (n\Delta\chi_1)^2 + \left( \frac{\bar{\chi}_1 - \bar{\chi}_0}{m+n} \right)^2 \left\{ (m\Delta\theta_0)^2 + (n\Delta\theta_1)^2 \right\} \right]^{\frac{1}{2}}, \quad (\text{A8}) \end{aligned}$$

where  $\bar{\chi}_k \equiv \bar{\chi}(\bar{p}_{i+k})$ ,  $\Delta\chi_k \equiv \Delta\chi(\bar{p}_{i+k})$ ,  $\bar{\theta}_k \equiv \bar{\theta}(\bar{p}_{i+k})$ ,  $\Delta\theta_k \equiv \Delta\theta(\bar{p}_{i+k})$ ,  $m = \bar{\theta}_1 - \theta$ , and  $n = \theta - \bar{\theta}_0$ . The first two terms in Eq. (A8) arise from the uncertainty in water measurements while the last term is due to the errors in potential temperature on sounding pressure levels. Equations (A7) and (A8) also apply to pressure and temperature to derive  $\bar{p}(\theta)$  and  $\bar{T}(\theta)$  together with  $\Delta p(\theta)$  and  $\Delta T(\theta)$  by replacing  $\chi$  with  $p$  and  $T$ , respectively. We apply these equations also to other variables such as ozone mixing ratio and geopotential height.

It is worth mentioning here that high resolution radiosondes do observe unstable atmospheric layers where the potential temperature does not increase monotonously with respect to altitude. In such cases, sounding pairs with  $\bar{\theta}_i \leq \theta \leq \bar{\theta}_{i+1}$  cannot be uniquely determined and the interpolation in Eq. (A7) and the estimation of uncertainties in Eq. (A8) could be made by using any sounding pairs with  $\bar{\theta}_i$  and  $\bar{\theta}_j$  that satisfy the conditions  $\bar{\theta}_i \leq \theta \leq \bar{\theta}_{i+1}$  and  $\bar{\theta}_{j-1} \leq \theta \leq \bar{\theta}_j$ . Since such unstable layers are subject to vertical mixing and large scale atmospheric features are better represented

by smooth sounding data, we avoid such ambiguity by choosing the pairs  $\bar{\theta}_i$  and  $\bar{\theta}_j$  that are found in the lowest altitude for  $\bar{\theta}_i$  and the highest altitude for  $\bar{\theta}_j$  that satisfy the above condition (Fig. 15). Usually this choice, at the same time, maximizes the estimated uncertainty in Eq. (A8) due to large values of  $(\bar{\chi}_1 - \bar{\chi}_0)^2$  multiplied by the uncertainty in potential temperature. We could thus avoid possible underestimation of observational uncertainties associated with the projection of observational data in unstable layers to isentropic coordinates.

### A3 Correction of the instrumental phase lag

CFH employs a sophisticated digital feedback controller, proportional/integral/derivative (PID) controller, to maintain constant frost on a mirror by cooling or heating it (Vömel et al., 2007a). Even with the use of such clever system, however, we cannot get rid of some phase delay in the observed values. For our practical purposes the PID parameters are not useful, while the response time is the simplest way to measure the delay. We use those values derived by extensive analyses having been made by Aqua Validation and Instrument Tests (AquaVIT) campaign (Fahey et al., 2009).

Instead of attempting to model the performance, here we make a brief consideration to apply it to our observed data. We assume that the output  $q(t)$  results from the convolution of the input  $p(t)$  with an  $e$ -folding time  $\tau$ :

$$q(t) = \frac{1}{W} \int_0^t p(s) e^{-\frac{t-s}{\tau}} ds, \quad (\text{A9})$$

$$W = \int_0^t e^{-\frac{t-s}{\tau}} ds = \tau(1 - e^{-\frac{t}{\tau}}). \quad (\text{A10})$$

Title Page

Abstract

Introduction

Conclusions

References

Tables

Figures

◀

▶

◀

▶

Back

Close

Full Screen / Esc

Printer-friendly Version

Interactive Discussion



During the continued operation in which  $t/\tau \gg 1$ ,

$$q(t) = \frac{1}{\tau} \int_0^t p(s) e^{-\frac{t-s}{\tau}} ds. \quad (\text{A11})$$

Differentiation of Eq. (A11) may lead to the differential form of the input-output relationship

$$\frac{dq(t)}{dt} = \frac{1}{\tau} (p(t) - q(t)), \quad (\text{A12})$$

which could be readily rearranged to give the unknown input  $p(t)$  from the instrumental output  $q(t)$ :

$$p(t) = q(t) + \tau \frac{dq(t)}{dt}. \quad (\text{A13})$$

If the value  $\tau$  is known, the input  $p(t)$ , here the atmospheric frostpoint temperature not affected by the instrumental phase delay, could be estimated from the output  $q(t)$ , here the observed mirror temperature. This formula is mathematically equivalent to the phase correction applied to the capacitance humidity sensors by Miloshevich et al. (2004).

Though incomplete, the application of Eq. (A13) to the observed profiles successfully reduced the phase difference between the ascending and the descending profiles as shown in Fig. 2. In most cases, the length of smoothing necessary for noise reduction is longer than that for compensation of the phase delay. The smoothing and phase correction parameters are summarized in Table 2.

## Appendix B

### Detailed description on the statistical nature of dehydration

Statistical features revealed in Fig. 14 are described by each isentrope trying to characterize the dehydration processes taking place in the TTL.

At 350 K potential temperature, plots are almost evenly scattered around the diagonal line, although relatively large uncertainties, suggestive of a bifurcation of backward trajectories (e.g. Hasebe et al., 2007, Fig. 1), exist especially those shown in blue (Bandung (BD) and Watukosek (WK)). As the convective motions easily reach 350 K in the tropics (Atticks and Robinson, 1983), the interpretation of the quasi symmetry along the diagonal line would not be that the OMR is controlled by the dehydration associated with the horizontal advection, but rather that it is mostly determined by the temperature at the time of the outflow from a convective system. The water content in this case reflects the coldness of the isentrope in the convective region; large water content in Tarawa (TR; red) will be due to the relatively low altitude of 350 K isentropic level combined with active convection in the region. The OMR becomes lower as the station moves westward to Biak (BI; green), Bandung (BD) and Watukosek (WK; blue), and further to Kototabang (KT; purple). Local convection is still high around these stations, but 350 K isentrope gradually rises toward the west along the equator, meaning that the SMR on 350 K tends to be lower toward the Western Pacific. The features found on 350 K level along the equator thus reflect the local meteorological condition of the stations. The dryness of Hanoi (HN; light blue) relative to other stations, on the other hand, requires a different consideration. This station is located in the subtropics where convective activity is not so high. It should also be emphasized that it is strongly affected by the outflow from the tropics, which leads to the seasonal minimum in the upper tropospheric ozone concentration during northern winter (Ogino et al., 2012).

On 360 K level, the majority of the points for the northern winter (NW) western tropical observations are found to the upper left side of the diagram beyond the critical

### TTL dehydration

F. Hasebe et al.

Title Page

Abstract

Introduction

Conclusions

References

Tables

Figures

◀

▶

◀

▶

Back

Close

Full Screen / Esc

Printer-friendly Version

Interactive Discussion



## TTL dehydration

F. Hasebe et al.

[Title Page](#)[Abstract](#)[Introduction](#)[Conclusions](#)[References](#)[Tables](#)[Figures](#)[◀](#)[▶](#)[◀](#)[▶](#)[Back](#)[Close](#)[Full Screen / Esc](#)[Printer-friendly Version](#)[Interactive Discussion](#)

supersaturation (dashed line), while those for SC (all season) and HN are still scattered around the diagonal. The uneven shift of the plots to the upper left side of the diagram indicates that the air parcels tend to contain more water than  $1.6 \times \text{SMR}_{\min}$ . It means that the dehydration is taking place for the air parcel on this isentrope during NW over the Western Tropical Pacific and that the dehydration does not occur immediately but takes some time before the water is removed to SMR. The driest parcels are found in the Western Pacific (BI, BD, WK) in general, but the OMR appears higher in KT as compared to other stations in the region. The  $\text{SMR}_{\min}$  is extremely low for some parcels reaching as low as 1 ppmv, which is much lower than the average in the lower stratosphere.

The removal of water from the advected air parcel continues on the isentrope 365 K. The features remain almost the same as those on 360 K except that both OMR and  $\text{SMR}_{\min}$  are smaller than those on 360 K. Most of the plots found below the diagonal line with relatively large uncertainties in OMR are those from the Eastern Pacific in March–May period in the late 1990s taken by using NOAA/FPH. Some of the plots for Hanoi are found apart from the diagonal line, suggesting that the cold trap dehydration is also functioning to those air parcels advected outward from the tropics.

The scatter plots become more succinctly distributed near the lower left corner of the diagram as the air parcels rise to reach 370 K isentrope. Majority of the plots are still found above the diagonal line, but the occasions in which  $\text{OMR} > 1.6 \times \text{SMR}_{\min}$  become less frequent, indicating that the dehydration is less effective than that at 360 and 365 K. The plots are mostly found with the OMR less than 4 ppmv implying that some extreme dehydration, excessive of the requirement for stratospheric dryness, has already taken place.

The plots gradually moves to the right on the diagram to sit around the diagonal line as the air parcels ascend to 380 K. On rare occasion found are the parcels beyond the critical limit of  $1.6 \times \text{SMR}_{\min}$ , indicating that the dehydration is almost over before the air parcels reach this isentrope. The mean value of OMR during NW calculated from those in BI, KT and TR is  $1.9 \pm 0.6$  ppmv (unbiased standard deviation), while that in NS

## TTL dehydration

F. Hasebe et al.

[Title Page](#)[Abstract](#)[Introduction](#)[Conclusions](#)[References](#)[Tables](#)[Figures](#)[◀](#)[▶](#)[◀](#)[▶](#)[Back](#)[Close](#)[Full Screen / Esc](#)[Printer-friendly Version](#)[Interactive Discussion](#)

available only in SC is  $4.2 \pm 0.3$  ppmv. These values must reflect the level of dehydration achievable during the horizontal advection. Their differences come from two aspects; one from the seasonal march and the other from the east-west contrast. The former constitutes the foundation of the tape recorder signal (Mote et al., 1996) appearing in the seasonal migration of the plots for SC ranging from  $\sim 2$  ppmv in NW to  $4 \sim 7$  ppmv in northern summer (NS) to fall. Unfortunately, the magnitude of seasonal variation in the Western Tropical Pacific is not available since our observations there are restricted to NW. The latter could be seen from the fact that the extreme low values of OMR observed in BI and KT are not found in SC.

The movement to the right on the diagram continues to 400 K, where almost all plots are found to the lower right of the diagonal line. The cold-trap dehydration along horizontal advection no longer functions on this isentrope, meaning that the dehydration must have completed sometime more than seven days before the air reaches 400 K surface. The NW-mean OMR for BI, KT and TR is  $2.8 \pm 0.6$  ppmv. The seasonal amplitude of the OMR is reduced as the extremely low OMRs such as those less than 1.5 ppmv found on 380 K disappear. It may suggest that some hydration processes such as those associated with the evaporation of once-condensed ice particles and/or irreversible mixing with humid air outside the TTL have occurred before the air reaches 400 K.

*Acknowledgements.* The authors express hearty gratitude to those colleagues in Instituto Nacional de Meteorología e Hidrología of Ecuador, Lembaga Penerbangan dan Antariksa Nasional of Indonesia, the Meteorological Office of Tarawa, Kiribati, and Aero-Meteorological Observatory of Hanoi, Vietnam for their invaluable contribution to realize campaign observations. The COBALD sonde was provided by Frank G. Wienhold of Eidgenössische Technische Hochschule (ETH) Zürich, Switzerland. This work was supported by the Japan Society for the Promotion of Science, Grant-in-Aid for Scientific Research (A) 15204043, 18204041, 21244072, and 22241004, and the Global Environment Research Program (A-1) and (A-071) of the Ministry of the Environment.

## References

- Atticks, M. G. and Robinson, G. D.: Some features of the structure of the tropical tropopause, Q. J. Roy. Meteor. Soc., 109, 295–308, 1983. 25850, 25861
- Brewer, A. W.: Evidence for a world circulation provided by the measurements of helium and water vapour distribution in the stratosphere, Q. J. Roy. Meteor. Soc., 75, 351–363, 1949. 25835
- Danielsen, E. F.: A dehydration mechanism for the stratosphere, Geophys. Res. Lett., 9, 605–608, 1982. 25836
- Eguchi, N. and Shiotani, M.: Intraseasonal variations of water vapor and cirrus clouds in the tropical upper troposphere, J. Geophys. Res., 109, D12106, doi:10.1029/2003JD004314, 2004. 25854
- Fahey, D. W., Gao, R. S., and Möhler, O.: Summary of the AquaVIT Water Vapor Intercomparison: Static Experiments, personal communications, available at: [http://cires.colorado.edu/~voemel/publications/AquaVITWhitePaper\\_Final\\_23Oct2009\\_22MB.pdf](http://cires.colorado.edu/~voemel/publications/AquaVITWhitePaper_Final_23Oct2009_22MB.pdf), last access: 6 August 2012, 2009. 25859
- Fueglistaler, S. and Haynes, P. H.: Control of interannual and longer-term variability of stratospheric water vapor, J. Geophys. Res., 110, D24108, doi:10.1029/2005JD006019, 2005. 25836
- Fueglistaler, S., Wernli, H., and Peter, T.: Tropical troposphere-to-stratosphere transport inferred from trajectory calculations, J. Geophys. Res., 109, D03108, doi:10.1029/2003JD004069, 2004. 25836
- Fueglistaler, S., Bonazzola, M., Haynes, P. H., and Peter, T.: Stratospheric water vapor predicted from the Lagrangian temperature history of air entering the stratosphere in the tropics, J. Geophys. Res., 110, D08107, doi:10.1029/2004JD005516, 2005. 25836
- Fueglistaler, S., Dessler, A. E., Dunkerton, T. J., Folkins, I., Fu, Q., and Mote, P. W.: Tropical Tropopause Layer, Rev. Geophys., 47, RG1004, doi:10.1029/2008RG000267, 2009. 25850
- Fujiwara, M., Hasebe, F., Shiotani, M., Nishi, N., Vömel, H., and Oltmans, S. J.: Water vapor control at the tropopause by equatorial Kelvin waves observed over the Galápagos, Geophys. Res. Lett., 28, 3143–3146, 2001. 25854
- Fujiwara, M., Shiotani, M., Hasebe, F., Vömel, H., Oltmans, S. J., Ruppert, P. W., Horinouchi, T., and Tsuda, T.: Performance of the Meteorolabor “Snow White” chilled-mirror hygrometer in the

### TTL dehydration

F. Hasebe et al.

Title Page

Abstract

Introduction

Conclusions

References

Tables

Figures

◀

▶

◀

▶

Back

Close

Full Screen / Esc

Printer-friendly Version

Interactive Discussion



## TTL dehydration

F. Hasebe et al.

Title Page

Abstract

Introduction

Conclusions

References

Tables

Figures

I◀

▶I

◀

▶

Back

Close

Full Screen / Esc

Printer-friendly Version

Interactive Discussion



tropical troposphere: comparisons with the Vaisala RS80 A/H-Humicap sensors, *J. Atmos. Ocean. Tech.*, 20, 1534–1542, 2003. 25836, 25840

Fujiwara, M., Iwasaki, S., Shimizu, A., Inai, Y., Shiotani, M., Hasebe, F., Matsui, I., Sugimoto, N., Okamoto, H., Nishi, N., Hamada, A., Sakazaki, T., and Yoneyama, K.: Cirrus observations in the Tropical Tropopause Layer over the Western Pacific, *J. Geophys. Res.*, 114, D09304, doi:10.1029/2008JD011040, 2009. 25838, 25854

Fujiwara, M., Vömel, H., Hasebe, F., Shiotani, M., Ogino, S.-Y., Iwasaki, S., Nishi, N., Shibata, T., Shimizu, K., Nishimoto, E., Canossa, J. M. V., Selkirk, H. B., and Oltmans, S. J.: Seasonal to decadal variations of water vapor in the tropical lower stratosphere observed with balloon-borne cryogenic frostpoint hygrometers, *J. Geophys. Res.*, 115, D18304, doi:10.1029/2010JD014179, 2010. 25836

Fujiwara, M., Polavarapu, S., and Jackson, D.: A proposal of the SPARC reanalysis/analysis intercomparison project, *SPARC Newsletter*, 38, 14–17, 2012. 25851

Goff, A. J. and Gratch, S.: Low-pressure properties of water from –160 to 212 °F, *Transactions American Society of Heating and Ventilating Engineers*, 52, 95–122, 1946. 25841

Hamada, A. and Nishi, N.: Development of a cloud-top height estimation method by geostationary satellite split-window measurements trained with *CloudSat* Data, *J. Appl. Meteorol. Clim.*, 49, 2035–2049, 2010. 25853

Hasebe, F.: Quasi-biennial oscillations of ozone and diabatic circulation in the equatorial stratosphere, *J. Atmos. Sci.*, 51, 729–745, 1994. 25839

Hasebe, F., Shiotani, M., Vömel, H., Fujiwara, M., Nishi, N., Niwano, M., Uetake, T., Ikeda, M., Ogawa, T., Oltmans, S. J., and Gage, K.: First results from the SOWER/Pacific 1998/1999 campaigns, in: *Atmospheric Ozone, Proceedings of the Quadrennial Ozone Symposium*, Sapporo, 3–8 July 2000, 783–784, 2000. 25836

Hasebe, F., Fujiwara, M., Nishi, N., Shiotani, M., Vömel, H., Oltmans, S., Takashima, H., Saraspriya, S., Komala, N., and Inai, Y.: In situ observations of dehydrated air parcels advected horizontally in the Tropical Tropopause Layer of the western Pacific, *Atmos. Chem. Phys.*, 7, 803–813, doi:10.5194/acp-7-803-2007, 2007. 25837, 25841, 25844, 25849, 25861

Holton, J. R. and Gettelman, A.: Horizontal transport and the dehydration of the stratosphere, *Geophys. Res. Lett.*, 28, 2799–2802, 2001. 25836

Inai, Y., Hasebe, F., Shimizu, K., and Fujiwara, M.: Correction of radiosonde pressure and temperature measurements using simultaneous GPS height data, *SOLA*, 5, 109–112, doi:10.2151/sola.2009-028, 2009. 25839

- Inai, Y., Hasebe, F., Fujiwara, M., Shiotani, M., Nishi, N., Ogino, S.-Y., Vömel, H., Iwasaki, S., and Shibata, T.: Dehydration in the Tropical Tropopause Layer estimated from the water vapor match, in preparation, 2012. 25837, 25849, 25853, 25855
- 5 Iwasaki, S., Maruyama, K., Hayashi, M., Ogino, S.-Y., Ishimoto, H., Tachibana, Y., Shimizu, A., Matsui, I., Sugimoto, N., Yamashita, K., Saga, K., Iwamoto, K., Kamiakito, Y., Chabangborn, A., Thana, B., Hashizume, M., Koike, T., and Oki, T.: Characteristics of aerosol and cloud particle size distributions in the tropical tropopause layer measured with optical particle counter and lidar, *Atmos. Chem. Phys.*, 7, 3507–3518, doi:10.5194/acp-7-3507-2007, 2007. 25852
- 10 Jensen, E. and Pfister, L.: Transport and freeze-drying in the tropical tropopause layer, *J. Geophys. Res.*, 109, D02207, doi:10.1029/2003JD004022, 2004. 25836
- Jensen, E. J., Toon, O. B., Selkirk, H. B., Spinhirne, J. D., and Schoeberl, M. R.: On the formation and persistence of subvisible cirrus clouds near the Tropical Tropopause, *J. Geophys. Res.*, 101, 21361–21375, 1996. 25836
- 15 Koop, T., Luo, B., Tsias, A., and Peter, T.: Water activity as the determinant for homogeneous ice nucleation in aqueous solutions, *Nature*, 406, 611–614, 2000. 25849, 25852
- Krämer, M., Schiller, C., Afchine, A., Bauer, R., Gensch, I., Mangold, A., Schlicht, S., Spelten, N., Sitnikov, N., Borrmann, S., de Reus, M., and Spichtinger, P.: Ice supersaturations and cirrus cloud crystal numbers, *Atmos. Chem. Phys.*, 9, 3505–3522, doi:10.5194/acp-9-3505-2009, 2009. 25848
- 20 Liu, Y. S., Fueglistaler, S., and Haynes, P. H.: Advection-condensation paradigm for stratospheric water vapor, *J. Geophys. Res.*, 115, D24307, doi:10.1029/2010JD014352, 2010. 25836, 25851
- Miloshevich, L. M., Paukkunen, A., Vömel, H., and Oltmans, S. J.: Development and validation of a time-lag correction for vaisala radiosonde humidity measurements, *J. Atmos. Ocean. Techn.*, 21, 1305–1327, 2004. 25860
- 25 Mote, P. W., Rosenlof, K. H., McIntyre, M. E., Carr, E. S., Gille, J. C., Holton, J. R., Kinnerson, J. S., Pumphrey, H. C., Russell III, J. M., and Waters, J. W.: An atmospheric tape recorder: the imprint of tropical tropopause temperatures on stratospheric water vapor, *J. Geophys. Res.*, 101, 3989–4006, 1996. 25863
- 30 Murphy, D. M. and Koop, T.: Review of the vapour pressures of ice and supercooled water for atmospheric applications, *Q. J. Roy. Meteor. Soc.*, 131, 1539–1565, 2005. 25841

## TTL dehydration

F. Hasebe et al.

[Title Page](#)[Abstract](#)[Introduction](#)[Conclusions](#)[References](#)[Tables](#)[Figures](#)[◀](#)[▶](#)[◀](#)[▶](#)[Back](#)[Close](#)[Full Screen / Esc](#)[Printer-friendly Version](#)[Interactive Discussion](#)

**TTL dehydration**

F. Hasebe et al.

[Title Page](#)[Abstract](#)[Introduction](#)[Conclusions](#)[References](#)[Tables](#)[Figures](#)[◀](#)[▶](#)[◀](#)[▶](#)[Back](#)[Close](#)[Full Screen / Esc](#)[Printer-friendly Version](#)[Interactive Discussion](#)

- Murray, F. W.: On the computation of saturation vapor pressure, *J. Appl. Meteorol.*, 6, 203–204, 1967. 25841
- Newell, R. E. and Gould-Stewart, S.: A stratospheric fountain?, *J. Atmos. Sci.*, 38, 2789–2796, 1981. 25836
- 5 Ogino, S.-Y., Fujiwara, M., Shiotani, M., Hasebe, F., Matsumoto, J., Hoang, T. H., and Thanh, N. T. T.: Ozone variations over the northern subtropical region revealed by ozonesonde observations in Hanoi, *J. Geophys. Res.*, in review, 2012. 25861
- Plumb, R. A. and Bell, R. C.: A model of the quasi-biennial oscillation on an equatorial beta-plane, *Q. J. Roy. Meteor. Soc.*, 108, 335–352, 1982. 25839
- 10 Popp, P. J., Marcy, T. P., Watts, L. A., Gao, R. S., Fahey, D. W., Weinstock, E. M., Smith, J. B., Herman, R. L., Troy, R. F., Webster, C. R., Christensen, L. E., Baumgardner, D. G., Voigt, C., Kärcher, B., Wilson, J. C., Mahoney, M. J., Jensen, E. J., and Bui, T. P.: Condensed-phase nitric acid in a tropical subvisible cirrus cloud, *Geophys. Res. Lett.*, 34, L24812, doi:10.1029/2007GL031832, 2007. 25852
- 15 Richard, E. C., Tuck, A. F., Aikin, K. C., Kelly, K. K., Herman, R. L., Troy, R. F., Hovde, S. J., Rosenlof, K. H., Thompson, T. L., and Ray, E. A.: High-resolution airborne profiles of CH<sub>4</sub>, O<sub>3</sub>, and water vapor near tropical Central America in late January to early February 2004, *J. Geophys. Res.*, 111, D13304, doi:10.1029/2005JD006513, 2006. 25836
- Schiller, C., Grooß, J.-U., Konopka, P., Plöger, F., Silva dos Santos, F. H., and Spelten, N.: Hydration and dehydration at the tropical tropopause, *Atmos. Chem. Phys.*, 9, 9647–9660, doi:10.5194/acp-9-9647-2009, 2009. 25852
- 20 Schoeberl, M. R. and Dessler, A. E.: Dehydration of the stratosphere, *Atmos. Chem. Phys.*, 11, 8433–8446, doi:10.5194/acp-11-8433-2011, 2011. 25836, 25851
- Selkirk, H. B., Vömel, H., Canossa, J. M. V., Pfister, L., Diaz, J. A., Fernández, W., Amador, J., Stolz, W., and Peng, G. S.: Detailed structure of the tropical upper troposphere and lower stratosphere as revealed by balloon sonde observations of water vapor, ozone, temperature, and winds during the NASA TCSP and TC4 campaigns, *J. Geophys. Res.*, 115, D00J19, doi:10.1029/2009JD013209, 2010. 25852, 25853
- 25 Shibata, T., Vömel, H., Hamdi, S., Kaloka, S., Hasebe, F., Fujiwara, M., and Shiotani, M.: Tropical cirrus clouds near cold point tropopause under ice supersaturated conditions observed by lidar and balloon-borne cryogenic frost point hygrometer, *J. Geophys. Res.*, 112, D03210, doi:10.1029/2006JD007361, 2007. 25837, 25838
- 30

## TTL dehydration

F. Hasebe et al.

[Title Page](#)[Abstract](#)[Introduction](#)[Conclusions](#)[References](#)[Tables](#)[Figures](#)[◀](#)[▶](#)[◀](#)[▶](#)[Back](#)[Close](#)[Full Screen / Esc](#)[Printer-friendly Version](#)[Interactive Discussion](#)

- Shibata, T., Hayashi, M., Naganuma, A., Hara, N., Hara, K., Hasebe, F., Shimizu, K., Komala, N., Inai, Y., Vömel, H., Hamdi, S., Iwasaki, S., Fujiwara, M., Shiotani, M., Ogino, S.-Y., and Nishi, N.: Cirrus cloud appearance in a volcanic aerosol layer around the tropical cold point tropopause over Biak, Indonesia in January 2011, *J. Geophys. Res.*, 115, D11209, doi:10.1029/2011JD017029, 2012. 25838
- 5 Vömel, H., Oltmans, S. J., Hofmann, D. J., Deshler, T., and Rosen, J. M.: The evolution of the dehydration in the Antarctic stratospheric vortex, *J. Geophys. Res.*, 100, 13919–13926, 1995. 25836
- Vömel, H., Oltmans, S. J., Johnson, B. J., Hasebe, F., Shiotani, M., Fujiwara, M., Nishi, N., Agama, M., Cornejo, J., Paredes, F., and Enriquez, H.: Balloon-borne observations of water vapor and ozone in the tropical upper troposphere and lower stratosphere, *J. Geophys. Res.*, 107, 4210, doi:10.1029/2001JD000707, 2002. 25836
- 10 Vömel, H., Fujiwara, M., Shiotani, M., Hasebe, F., Oltmans, S. J., and Barnes, J. E.: The behavior of the Snow White chilled-mirror hygrometer in extremely dry conditions, *J. Atmos. Ocean. Tech.*, 20, 1560–1567, 2003. 25836
- Vömel, H., David, D. E., and Smith, K.: Accuracy of tropospheric and stratospheric water vapor measurements by the cryogenic frost point hygrometer: instrumental details and observations, *J. Geophys. Res.*, 112, D08305, doi:10.1029/2006JD007224, 2007a. 25836, 25840, 25857, 25859
- 15 Vömel, H., Yushkov, V., Khaykin, S., Korshunov, L., Kyrö, E., and Kivi, R.: Intercomparisons of stratospheric water vapor sensors: FLASH-B and NOAA/CMDL frost-point hygrometer, *J. Atmos. Ocean. Techn.*, 24, 941–952, 2007b. 25840, 25851
- Winker, D. M. and Trepte, C. R.: Laminar cirrus observed near the tropical tropopause by LITE, *Geophys. Res. Lett.*, 25, 3351–3354, 1998. 25836

## TTL dehydration

F. Hasebe et al.

**Table 1.** Summary of water vapour sonde observations during each campaign. Only those with NOAA Frostpoint Hygrometer (FPH) and Cryogenic Frostpoint Hygrometer (CFH) are shown. See Fig. 1 for geographical location.

	Hanoi	Kototabang	Bandung	Watukosek	Biak	Tarawa	San Cristobal
Lat.	21.0	-0.2	-6.9	-7.6	-1.2	1.4	-0.9
Lon.	105.8	100.3	107.6	112.7	136.1	172.9	-89.6
1998	–	–	–	–	–	–	3 (Mar/Apr), 3 (Sep)
1999	–	–	–	–	–	–	3 (Mar), 3 (Sep/Oct)
2000	–	–	–	–	–	–	6 (Nov/Dec)
2001	–	–	–	5 (Nov/Dec)	–	–	–
2002	–	–	–	–	–	–	2 (Aug)
2003	–	–	4 (Dec)	3 (Jan)	–	–	1 (Mar)
2004	–	–	4 (Dec)	–	–	–	2 (Jul)
2005	–	–	–	–	–	2 (Dec)	–
2006	–	–	–	–	9 (Jan)	–	–
2007	6 (Jan)	5 (Jan)	–	–	6 (Jan)	5 (Jan)	–
2008	5 (Jan)	4 (Jan)	–	–	7 (Jan)	–	–
2009	4 (Jan)	–	–	–	4 (Jan)	–	–

Title Page

Abstract

Introduction

Conclusions

References

Tables

Figures

I◀

▶I

◀

▶

Back

Close

Full Screen / Esc

Printer-friendly Version

Interactive Discussion





## TTL dehydration

F. Hasebe et al.

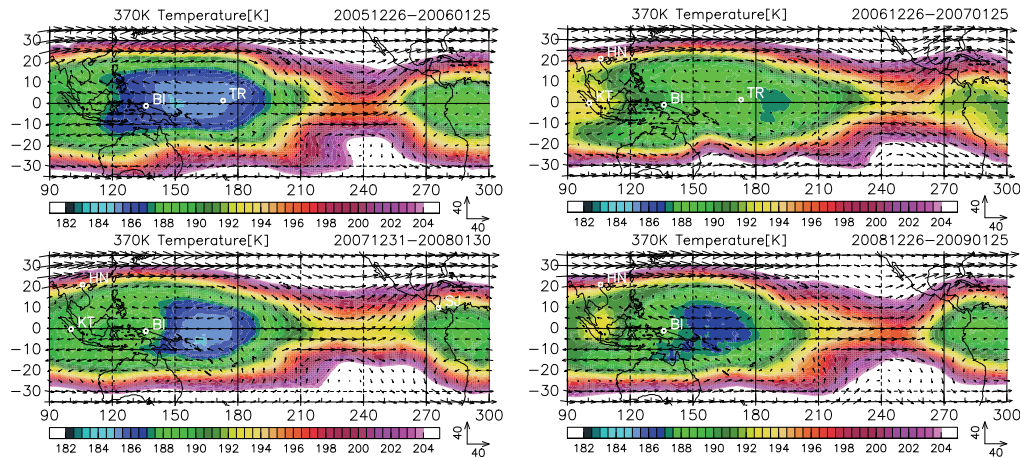


**Fig. 1.** Latitude-longitude sections of the mean horizontal wind component (vectors; scales of  $40 \text{ m s}^{-1}$  at the bottom right) and temperature (color) on 370 K isentropic surface during four SOWER campaigns. The averages are taken for 31 days covering the primary campaign period. Ground stations operated during the corresponding period, Tarawa (TR), Biak (BI), Kototabang (KT), and Hanoi (HN), are indicated.

Title Page

Abstract

Introduction

Conclusions

References

Tables

Figures

◀

▶

◀

▶

Back

Close

Full Screen / Esc

Printer-friendly Version

Interactive Discussion



## TTL dehydration

F. Hasebe et al.

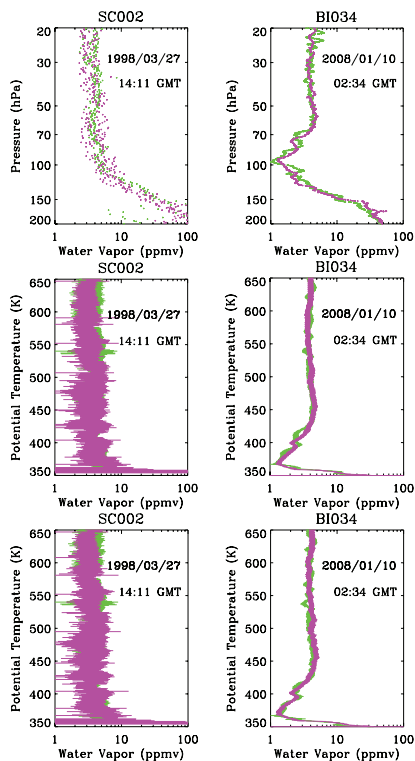


**Fig. 2.** Examples of water mixing ratio (ppmv) profiles taken at (left) San Cristóbal (SC) in March 1998 and (right) Biak (BI) in January 2008. Ascending (green) and descending (purple) profiles are superposed to visualize the phase delay associated with the upward and downward sonde motion. (Top) raw data, (middle) same data projected on isentropic coordinates, and (bottom) same with phase correction applied. See Appendix for the data processing procedure and the derivation of uncertainties shown in horizontal bars.

Title Page

Abstract

Introduction

Conclusions

References

Tables

Figures



Back

Close

Full Screen / Esc

Printer-friendly Version

Interactive Discussion



## TTL dehydration

F. Hasebe et al.

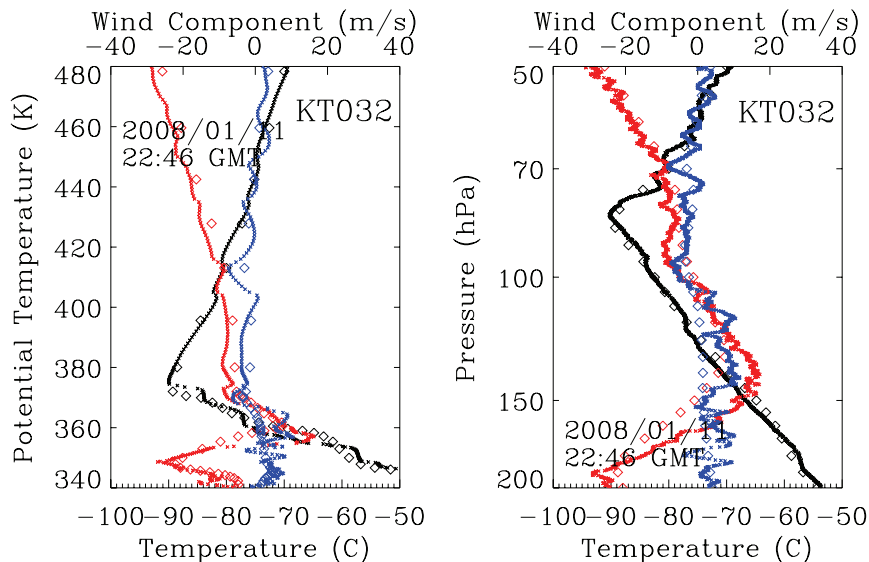


**Fig. 3.** Profiles of temperature (black) and zonal (red) and meridional (blue) wind components as a function of (left) pressure (hPa) and (right) potential temperature (K) at Kototabang observed on 11 January 2008. Radiosonde observations (densely populated crosses) and corresponding ECMWF analysis interpolated to the station (diamonds) are compared.

Title Page

Abstract

Introduction

Conclusions

References

Tables

Figures

◀

▶

◀

▶

Back

Close

Full Screen / Esc

Printer-friendly Version

Interactive Discussion



## TTL dehydration

F. Hasebe et al.

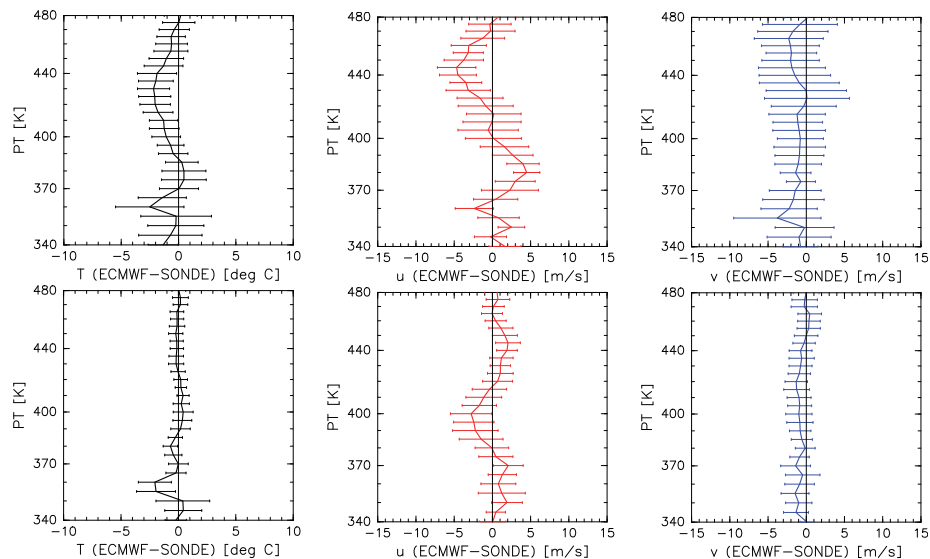


**Fig. 4.** Ensemble mean differences of (left) temperature and (center) zonal and (right) meridional wind components between radiosonde observations and ECMWF analysis illustrated as a function of potential temperature. Estimations are made by using SOWER station data at Tarawa, Biak, Bandung and Kototabang for the period (top) before and (bottom) after December 2006. The horizontal bars correspond to the confidence interval of 99 %.

[Title Page](#)[Abstract](#)[Introduction](#)[Conclusions](#)[References](#)[Tables](#)[Figures](#)[◀](#)[▶](#)[◀](#)[▶](#)[Back](#)[Close](#)[Full Screen / Esc](#)[Printer-friendly Version](#)[Interactive Discussion](#)

**TTL dehydration**

F. Hasebe et al.

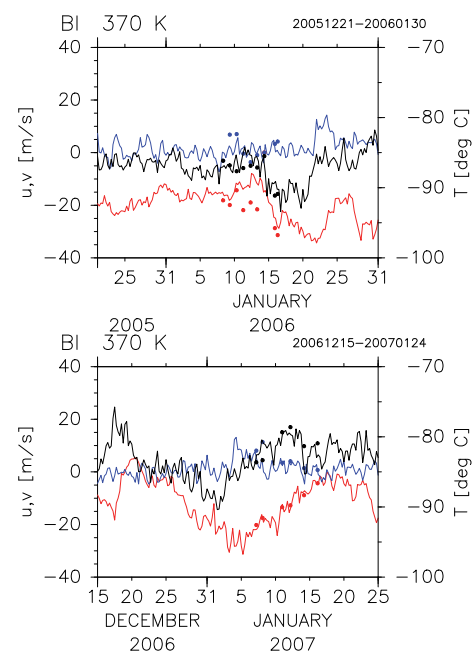


**Fig. 5.** Time series of temperature (black) and zonal (red) and meridional (blue) wind components based on 6-h interval ECMWF analysis interpolated to 370 K potential temperature level at Biak station for the period (top) from 21 December 2005 to 31 January 2006 and (bottom) from 15 December 2006 to 25 January 2007. Sonde observations are superposed by dots.

Title Page

Abstract Introduction

Conclusions References

Tables Figures

◀ ▶

◀ ▶

Back Close

Full Screen / Esc

Printer-friendly Version

Interactive Discussion



## TTL dehydration

F. Hasebe et al.

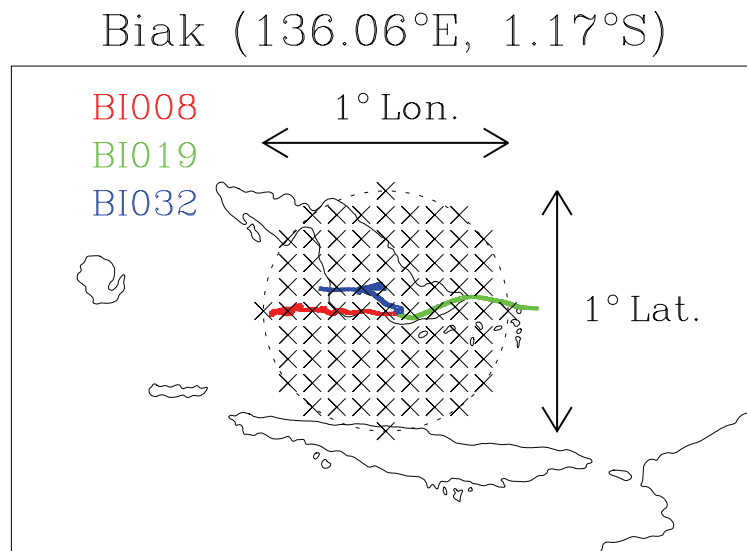


**Fig. 6.** Initial location of air segments set for calculating backward trajectories distributed with an interval of  $0.1^{\circ}$  in a diameter of  $1^{\circ}$  centered at Biak sonde station. Underlying solid curves are the horizontal projection of three sonde flight tracks drawn for the purpose of reference.

[Title Page](#)[Abstract](#)[Introduction](#)[Conclusions](#)[References](#)[Tables](#)[Figures](#)[◀](#)[▶](#)[◀](#)[▶](#)[Back](#)[Close](#)[Full Screen / Esc](#)[Printer-friendly Version](#)[Interactive Discussion](#)

## TTL dehydration

F. Hasebe et al.

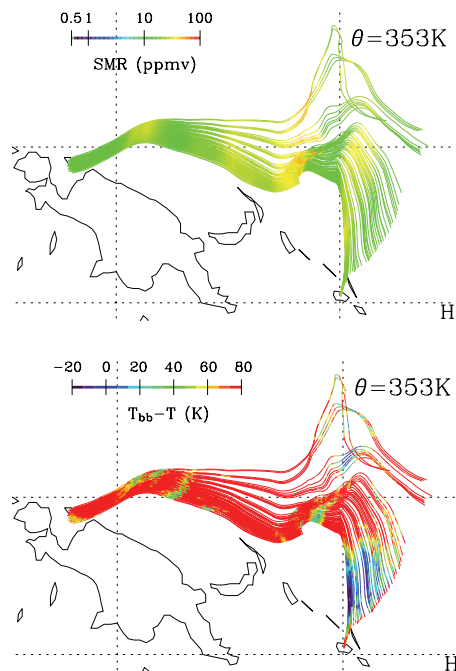


**Fig. 7.** Seven-day isentropic backward trajectories started from Biak (left end) on 353 K surface corresponding to the sounding on 8 January 2006. Trajectories are color-coded by (top) saturation mixing ratio estimated from ECMWF analysis and (bottom) the difference between the equivalent blackbody temperature (brightness temperature)  $T_{bb}$  observed by geostationary satellite and the temperature  $T$  of the advected air parcel.

## TTL dehydration

F. Hasebe et al.

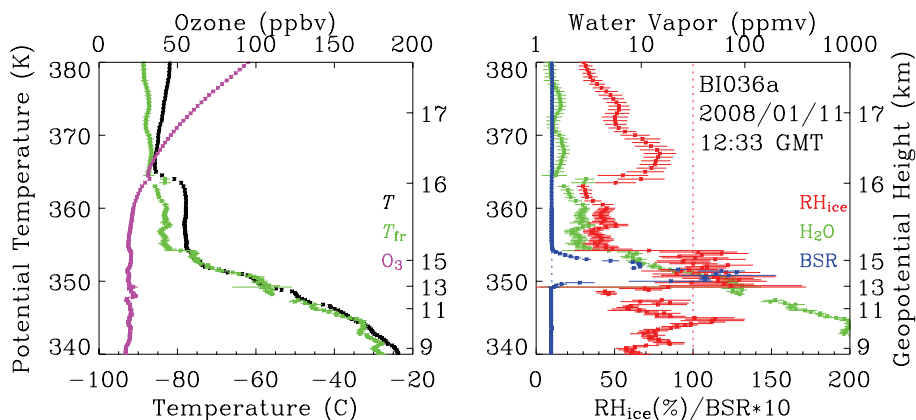


**Fig. 8.** Vertical profiles of (left) temperature (black; °C), frostpoint temperature observed by CFH ( $T_{fr}$ ; green; °C), and ozone mixing ratio (purple; ppbv in upper scale), and (right) water mixing ratio converted from  $T_{fr}$  shown on the left (green; ppmv in upper scale), relative humidity with respect to ice ( $RH_{ice}$ ; red; %), and backscattering ratio (BSR) observed by COBALD (blue channel: 455 nm) multiplied by 10 (blue) taken from the ascending portion of the sounding launched at 12:33 GMT on 11 January 2008 at Biak. Horizontal bars are the estimated uncertainties as described in Appendix A2. Dashed vertical lines on the right panel correspond to 100 % in  $RH_{ice}$  (red) and 1 in BSR (blue).

[Title Page](#)
[Abstract](#)
[Introduction](#)
[Conclusions](#)
[References](#)
[Tables](#)
[Figures](#)
[◀](#)
[▶](#)
[◀](#)
[▶](#)
[Back](#)
[Close](#)
[Full Screen / Esc](#)
[Printer-friendly Version](#)
[Interactive Discussion](#)


## TTL dehydration

F. Hasebe et al.

Title Page

Abstract

Introduction

Conclusions

References

Tables

Figures

◀

▶

◀

▶

Back

Close

Full Screen / Esc

Printer-friendly Version

Interactive Discussion

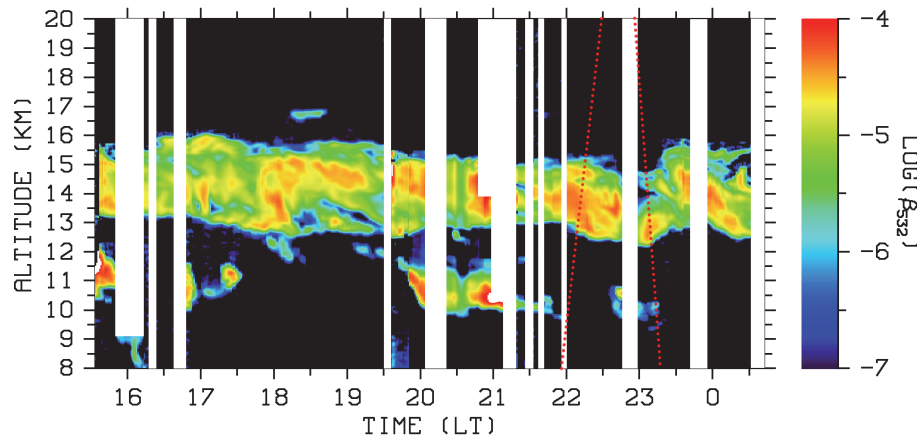


**Fig. 9.** Time-height section of the backscattering coefficient ( $\text{m}^{-1} \text{str}^{-1}$ ) at 532 nm observed by the Biak lidar. Red dotted lines: superposed ascending and descending sonde flight tracks. White bands: periods with low data quality. Local time at Biak shown in abscissa is GMT + 9. The range in which the COBALD BSR exceeds 10 in Fig. 8 corresponds to altitudes between 13.2 and 15.0 km.

## TTL dehydration

F. Hasebe et al.

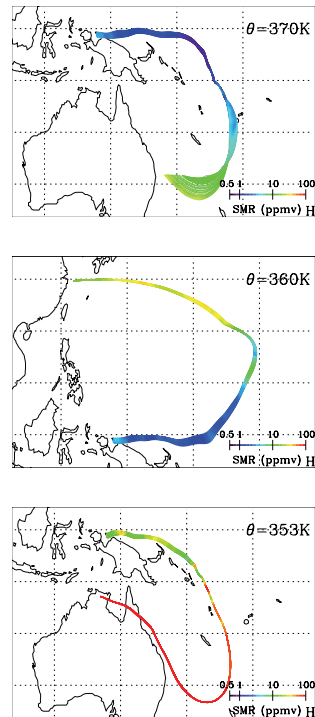


**Fig. 10.** Seven-day isentropic backward trajectories started from Biak on (top) 370, (middle) 360, and (bottom) 353 K surfaces corresponding to the observation shown in Fig. 8. Trajectories are color-coded by saturation mixing ratio estimated from ECMWF analysis.

[Title Page](#)[Abstract](#)[Introduction](#)[Conclusions](#)[References](#)[Tables](#)[Figures](#)[◀](#)[▶](#)[◀](#)[▶](#)[Back](#)[Close](#)[Full Screen / Esc](#)[Printer-friendly Version](#)[Interactive Discussion](#)

## TTL dehydration

F. Hasebe et al.

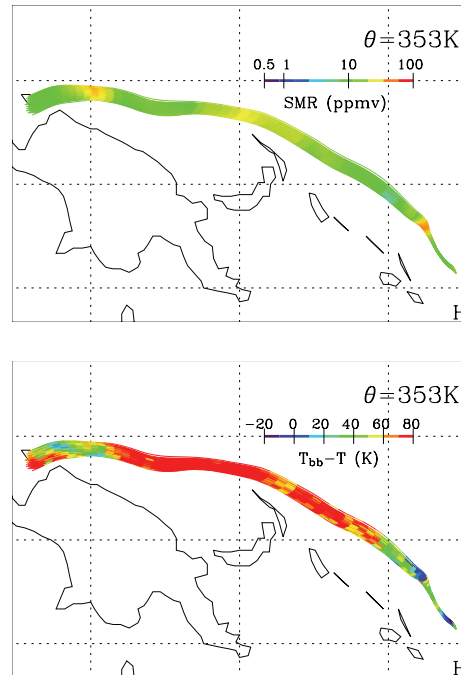


**Fig. 11.** (Top) the same as the bottom panel (353 K) of Fig. 10 but for three-day portion of the backward trajectories, and (bottom) the same but color-coded by the difference between the equivalent blackbody temperature  $T_{bb}$  observed by geostationary satellite and the air temperature  $T$ . Dark colors indicate penetrating convective clouds while warm colors cloud-free air at or above trajectory.

Title Page

Abstract

Introduction

Conclusions

References

Tables

Figures

◀

▶

◀

▶

Back

Close

Full Screen / Esc

Printer-friendly Version

Interactive Discussion



## TTL dehydration

F. Hasebe et al.

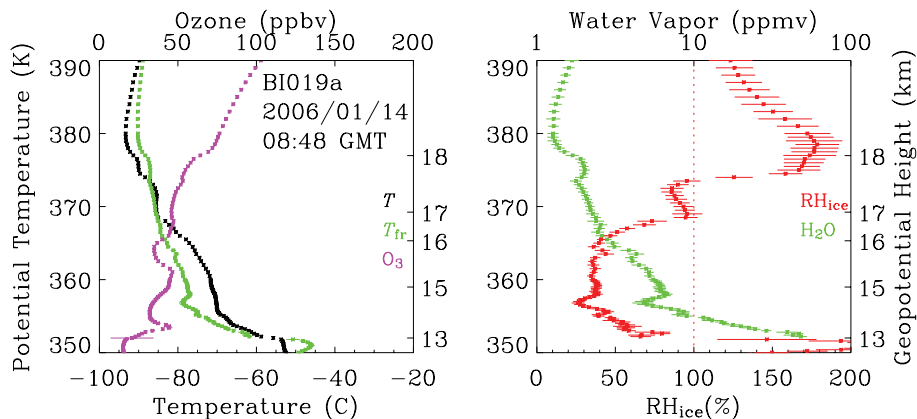


**Fig. 12.** The same as Fig. 8 but for the launch conducted at 8:48 GMT on 14 January 2006. Note that the vertical range is from 350 to 390 K rather than 340 to 380 K as in Fig. 8. COBALD data are not available at the time of this observation.

[Title Page](#)
[Abstract](#)
[Introduction](#)
[Conclusions](#)
[References](#)
[Tables](#)
[Figures](#)
[◀](#)
[▶](#)
[◀](#)
[▶](#)
[Back](#)
[Close](#)
[Full Screen / Esc](#)
[Printer-friendly Version](#)
[Interactive Discussion](#)


**TTL dehydration**

F. Hasebe et al.

Title Page

Abstract

Introduction

Conclusions

References

Tables

Figures

◀

▶

◀

▶

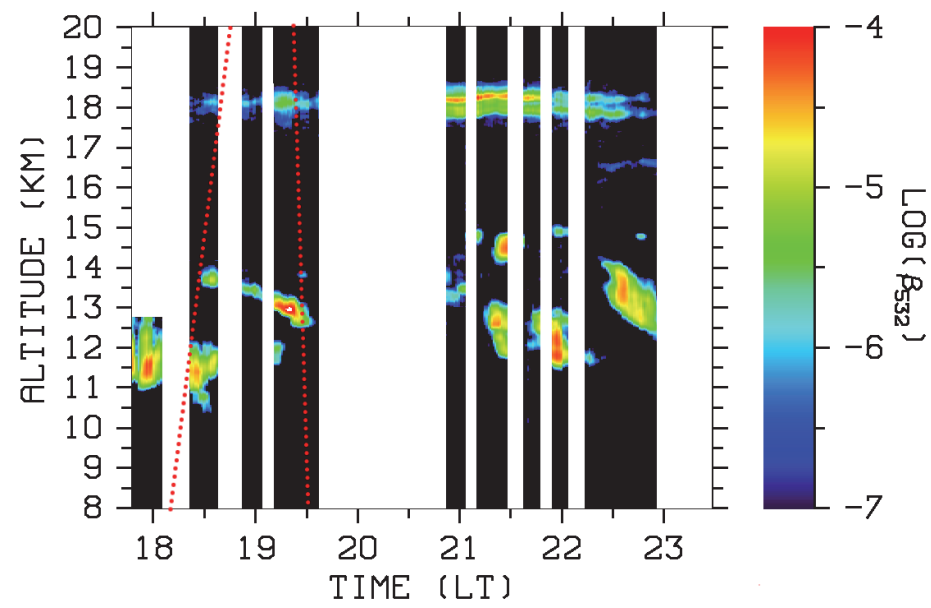
Back

Close

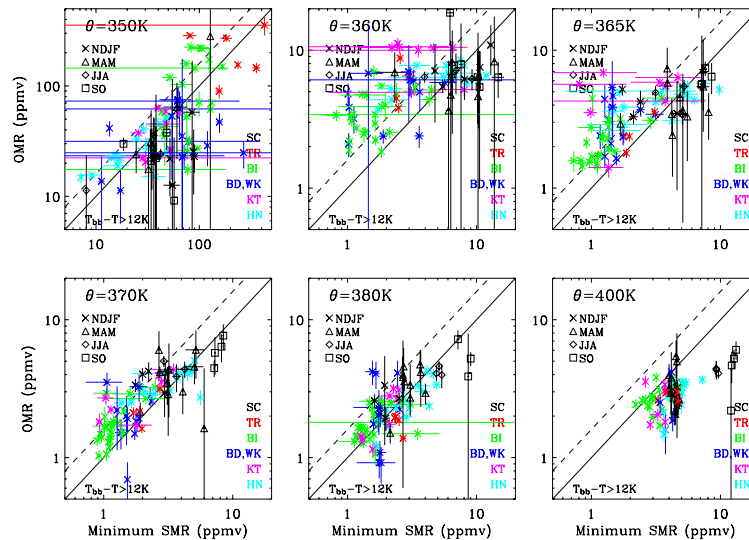
Full Screen / Esc

Printer-friendly Version

Interactive Discussion

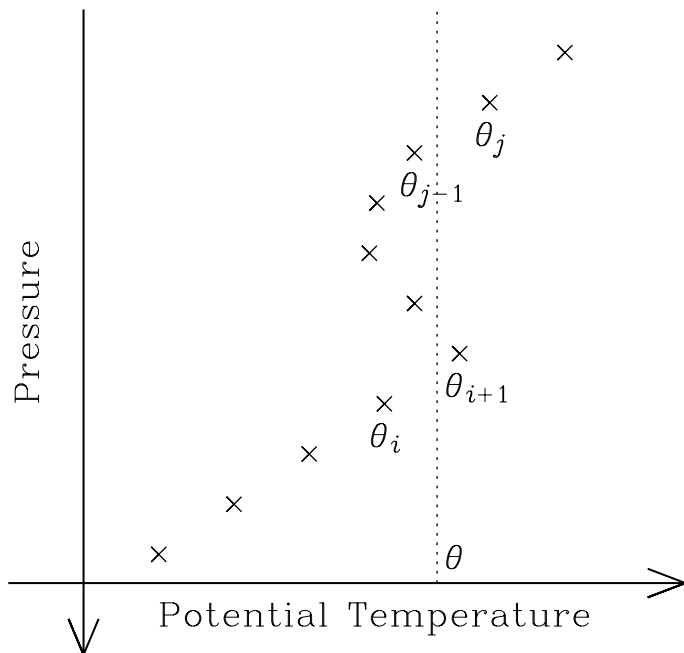


**Fig. 13.** The same as Fig. 9 but for 14 January 2006. Dotted red lines: ascent and descent of the sounding shown in Fig. 12.



**Fig. 14.** Scatter diagrams of the minimum saturation mixing ratio ( $SMR_{\min}$ ) experienced within seven days before the sounding and the observed value (OMR) on six isentropic levels ( $\theta = 350\text{--}400\text{ K}$ ). Diagonal line:  $OMR = SMR_{\min}$ , i.e. complete dehydration to the value expected from the minimum along the trajectory. Dashed line:  $OMR = 1.6 \times SMR_{\min}$  allowing 60% supersaturation with respect to ice to include homogeneous ice nucleation. In case the advected air parcel is supposed to encounter deep convection ( $T_{bb} - T > 12\text{ K}$ ),  $SMR_{\min}$  is sought from those portions of trajectories after such events. Symbols refer to the seasons: San Cristóbal (SC) located in the eastern, Tarawa (TR) in the central, and Biak (BI), Bandung (BD), Watukosek (WK) and Kototabang (KT) in the Western Tropical Pacific, while Hanoi (HN) is in the northern subtropics (Table 1). The vertical bars: estimates of errors in sonde data (Appendix). Horizontal bars: estimates of  $SMR_{\min}$  deduced from the standard deviation of SMR for segments composed of the air parcel at the time the SMR assumes the minimum. Note different scale for 350 K (top left panel).

[Title Page](#)
[Abstract](#)
[Introduction](#)
[Conclusions](#)
[References](#)
[Tables](#)
[Figures](#)
[◀](#)
[▶](#)
[◀](#)
[▶](#)
[Back](#)
[Close](#)
[Full Screen / Esc](#)
[Printer-friendly Version](#)
[Interactive Discussion](#)

**Fig. 15.** Schematic illustration of interpolation to an isentropic surface  $\theta$  located in an inversion layer encountered by radiosonde observations (crosses). Linear interpolation will be made by using data pairs with  $\theta_i$  and  $\theta_j$  in this case.

**TTL dehydration**

F. Hasebe et al.

Title Page	
Abstract	Introduction
Conclusions	References
Tables	Figures
◀	▶
◀	▶
Back	Close
Full Screen / Esc	
Printer-friendly Version	
Interactive Discussion	

